F 4 X-ray Absorption Spectroscopy

L. Baumgarten
Peter Grünberg Institut
Forschungszentrum Jülich GmbH

Contents

1 Introduction

In x-ray absorption spectroscopy (XAS) the sample is irradiated with monochromatic x-rays of energy hν. One scans the radiation energy and observes the absorption. When the energy is sufficient to excite an electron from a core level to above the Fermi level a jump in the absorption cross section is observed. Discrete structures can be observed just above the threshold. They are divided into the x-ray absorption near edge structure (XANES) and the extended x-ray absorption fine structure (EXAFS). In an atom one expects a few sharp (discrete) lines just above the threshold, followed by a continuum. XANES is a probe of the local environment of an atom or of the unoccupied density of electronic states (in accordance with selection rules).

Traditionally XAS spectra are measured in transmission mode. The spectrum is given by the ratio of the intensity before and after the absorber. Since a core hole created by the absorption of a x-ray photon will decay either by x-ray emission (emission of a photon of lower energy) or by emission of an Auger electron, both decay channels can as well used as a measure of the absorption strength. For low x-ray photon energies the preferred method of detection is that of the photo yield. If the absorption length is much larger as the escape depth of electrons or fluorescent radiation, this signal is proportional to the fraction of the incident radiation absorbed in the surface region.

X-ray absorption spectroscopy is element specific and can likewise be applied to gases, liquids, and solids. Almost any material like catalysts, minerals, and biological tissue (in its natural aqueous environment) can be investigated. It can be used to study surfaces, interfaces, buried layers and impurities at low concentrations. Special techniques have been developed to study magnetic layers and magnetic nanostructures, which are now widely used in magnetic storage devices and magnetic sensors.

X-ray absorption needs intense tunable X-rays. Therefore, today, the synchrotron is exclusively used as a source [1]. Other like XPS and Auger Spectroscopy it does not depend on ultrahigh vacuum conditions. In contrast to XPS which due to the limited escape depth of the photoelectrons is restricted to near surface areas it is feasible to also investigate subsurface structures like buried interfaces in semiconductors devices or GMR-sensors. A variety of books have appeared on the field of which only a few can be mentioned [3-7]. Varies aspects of this contribution have also been dealt with in earlier Spring Schools of this series [8-14]. The historical development of the field is described in ref. [15].

In the next chapter I will recall some basic X-ray features, then in chapter 3 I will discuss the near edge structures (XANES). The XANES, also called NEXAFS, probes the projected electronic density of empty states (local partial density of States LPDOS) and the valence of absorber atoms. In chapter 4 the EXAFS, which probe the interatomic distances and the coordination number will be briefly described. Chapters 5 and 6 are devoted to X-ray magnetic circular dichroism (XMCD) and x-ray magnetic linear dichroism (XMLD). These address special methods that have been developed to study magnetic films and nanoparticles. They are the prerequisite for the photoelectron emission microscopy (PEEM), which allows the study of magnetic domains and the dynamics of magnetic particles on the nm scale [16].

2 Some X-ray Basics

Traditionally an X-ray absorption spectrum is obtained from the ratio of the beam intensities in front and behind the absorber while the photon energy is tuned. Since X-rays are electromagnetic waves their absorption in a homogeneous material is described by the Lambert-Beer's law:

$$I = I_0 e^{-\mu x}. \tag{1}$$

Here I_0 is the incident X-ray intensity and I is the remaining intensity after the beam has propagated the distance x inside the sample. The linear absorption coefficient $\mu = \mu(n\omega)$ depends on the energy of the x-ray photons and is related to the absorption cross section $\sigma(n\omega)$ $[\mathrm{cm}^2/\mathrm{atom}]$ as

$$\mu = \frac{\rho N_A}{A}\sigma \tag{2}$$

where ρ is the density of the target material, N_A is Avogadro's number and A is the atomic weight of the target material. To get a quantity that is independent on the target density the mass attenuation coefficient $\mu_m = \mu/\rho$ is often given. For mixed targets the mass attenuation coefficient can be calculated by summation of the contribution of the individual constituents.

$$\frac{\mu}{\rho} = \sum_i \left(\frac{\mu}{\rho}\right)_i c_i \tag{3}$$

where c_i is the weight concentration of the respective absorber atoms.

Four basic effects can contribute to the X-ray attenuation. These are the photoelectric absorption, the elastic (Rayleigh, Thompson) and the inelastic (Compton) scattering, and at energies above 1.022 MeV the electron-positron pair production. In the spectral range of interest here the photoelectric excitation is the dominant process, and we will consider only this contribution. Fig.1 shows the absorption coefficient at the L and K edges of a Cu-foil and in more detail the absorption fine structure in the vicinity of the K -edge.

In most of the spectral range plotted the attenuation coefficient decreases with increasing photon energy, approximately $\propto 1/(n\omega)^3$, except for certain points where it raises drastically. It is the vicinity of such "absorption edges" that we will study in some detail below. Except for the edges, the absorption coefficient is a smooth function of energy, with a value that depends on the sample density, the atomic number Z, atomic mass A, and the x-ray energy E roughly as

$$\mu \approx \frac{\rho Z^4}{A E^3} \tag{4}$$

For practical purposes it is often fit to so called victoreen functions [17] of the form

$$\mu(\lambda) = a \cdot \lambda^3 - b \cdot \lambda^4 \tag{5}$$

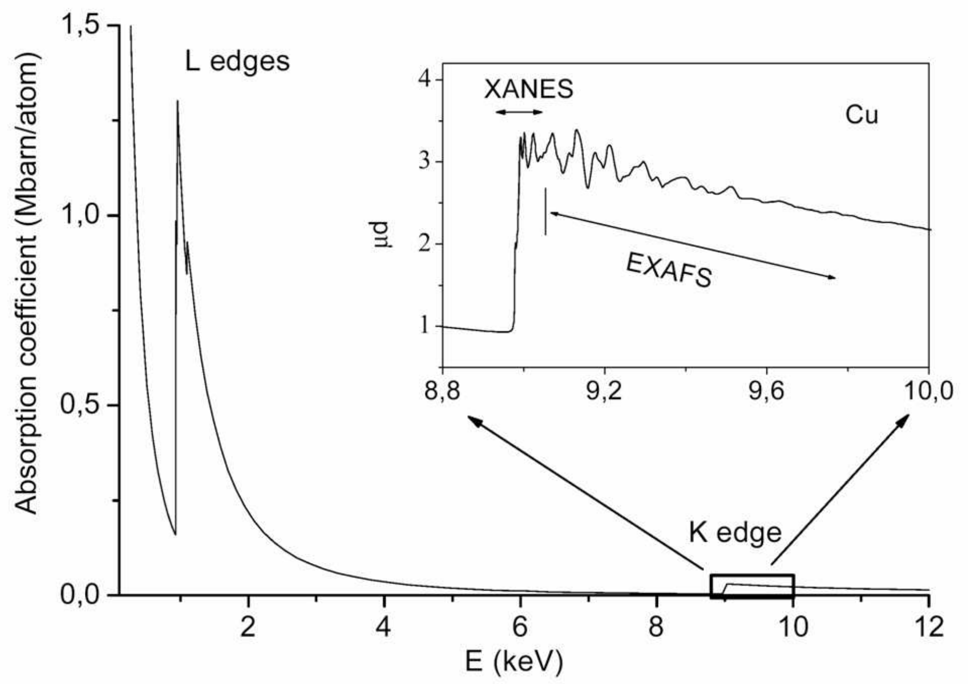

Fig. 1: *X-ray absorption coefficient of copper in the region of the* L *and* K *edges. The inset shows an expanded view of the* K *-edge region with the separation into a XANES and an EXAFS range [30].*

At the edges the photon energy reaches a value that is sufficient to excite an electron from a strongly bound core level to some high energy unoccupied state. With increasing energy it will even be ejected beyond the ionization limit into the continuum of states. The edges are denoted by letters K, L, M, . . . beginning this sequence with the edge of the highest energy. The K -edge is assigned to the excitation of a 1s-core level electron, the L_1 -edge to excitation of a 2s-electron, the L_2 and L_3 -edges to spin-orbit split $2p_{1/2}$ and $2p_{3/2}$ levels and so on for $M_1, \ldots, M_5, \ldots$.

The inset in fig. 1 shows the absorption coefficient in the vicinity of the K -edge of a Cu-foil in more detail. Such spectra are usually decomposed into three parts: The first part is the so called ”pre-edge” region which contains the background due to lower energy absorption transitions and sometimes also weak but specific absorption features to be discussed below. The second part is the XANES (X-ray Absorption Near Edge Structure) or NEXAFS (Near-Edge X-ray Absorption Fine Structure) - which basically means the same and includes the actual edge and the area to about 30eV beyond the edge. Because of the dipole selection rules XANES (NEXAFS) probes the projected electronic density of empty states (local partial density of States LPDOS) and the valence of the absorber atoms.

The third region is the EXAFS (Extended X-ray Absorption Fine Structure) range, which may extend to about 1000eV beyond the edge and essentially contains structural information about the immediate neighborhood of the absorber atom. EXAFS probes the coordination number and the interatomic distance.

In the literature the basics of the excitation processes are often visualized in terms of a simple single particle picture (independent electron approach). Although this is convenient for discussion one has to be careful with such a model. For a quantitative interpretation and an understanding of finer details a consideration of electron correlation effects is indispensable.

The simple single particle picture cannot even properly explain the splitting of the 2p levels (L_2 and L_3 edges). The reason lies in the fact that the spin-orbit splitting of the 2p-levels is a "final state effect" rather than an "initial state effect"; that is to say, that in the initial state the 2p-electrons are in a $2p^6$ closed sub-shell configuration. In this closed shell configuration the angular momentum is completely canceled and, thus, there is no spin-orbit interaction. To understand the level splitting we have to argue in a more proper configuration picture [19] as follows: X-ray transitions - like other optical transitions are usually electric dipole transitions [1]. We therefore have to consider the following selection rules for excitations to be allowed:

$$\begin{array}{ll} \Delta \mathrm{l} = \pm 1 & \Delta \mathrm{L} = 0, \pm 1 \\ \Delta \mathrm{m_l} = 0, \pm 1 & \Delta \mathrm{S} = 0 \\ \Delta \mathrm{m_s} = 0 & \Delta \mathrm{J} = 0, \pm 1, \\ \Delta \mathrm{j} = 0, \pm 1 & \text{not allowed } 0 \longleftrightarrow 0 \end{array}$$

For the 2p levels p → s and p → d transitions are allowed. Due to Fermis Golden Rule the transition probability per unit time from an initial state |i> to a final state |f> is

$$P_{if} = \frac{2\pi}{\hbar} |\langle f | \boldsymbol{\epsilon} \cdot \mathbf{r} | i \rangle|^2 \rho_f(E) \tag{6}$$

where $\boldsymbol{\epsilon}$ is the polarization vector of the electromagnetic wave and $\boldsymbol{\epsilon} \cdot \mathbf{r}$ is the interaction operator in the dipole approximation. $\rho_f(E)$ is the energy density of final states. This equation is derived from time dependent perturbation theory for an atom that is loosely coupled to a classical radiation field [20]. The X-ray field is treated as a classical plain wave.

In a metal the edge transitions occur to final states just above the Fermi level [2]. For a transition metal, like Pt, with an incompletely filled d-electronic shell we therefore expect a dominance of the d-final states over the s-final states. Because of this dominance of d states we will ignore here the p → s transitions. Thus, in a configuration picture the initial state can be described by a $2p^6 5d^9$ configuration. Alternatively, because of the cancellation of the angular momenta in a completely filled shell, this initial state can also be described as a d^1 hole configuration of the d states. The final state $2p^5 5d^{10}$ has a closed d-shell and can be described as a p^1 hole configuration of the 2p states. A $L_{2,3}$ -edge transition is then a d → p hole transition from a

---

[1] Quadrupole transitions are occasionally observed but weak in intensity.

[2] The Pauli-exclusion principle does not allow electrons to be excited into occupied states.

[3] Here again we have a single particle picture. This time with a d hole ground state and a p hole excited state. In

[2] The Pauli-exclusion principle does not allow electrons to be excited into occupied states.

$5d^1$ to a $2p^1$ hole configuration [3]. In this final state we have an incompletely filled 2p shell, which naturally will show spin-orbit interaction. The spin- orbit splitting of the p shell is therefore a “final state effect”. In a Russell-Saunders coupling scheme the L_3 - and L_2 -edges then correspond to $^2D \longrightarrow {}^2P_{3/2}$ and $^2D \longrightarrow {}^2P_{1/2}$ transitions, respectively. Note, that in this scheme the $J = 3/2$ state has the lower energy as required by the Hund’s rules [19]. Despite this described shortcoming of the single particle picture it is widely used in the literature to display the X-ray transitions, and we will also do so in the following.

The energetic position of the individual absorption edges increases with the atomic number approximately according to Moseleys law [21]:

$$\nu = C(Z - \sigma)^2 \tag{7}$$

where σ is a screening constant ($\sigma = 1.13$ for the K -shell and $\sigma \approx 7.9$ for the L - shell). That is, the higher the number of nuclear charges the stronger bound are the core electrons and the more energy will be needed to excite an electron to an empty valence state. This and the fact that the energies are so well defined makes X-ray spectroscopy so element specific.[4]

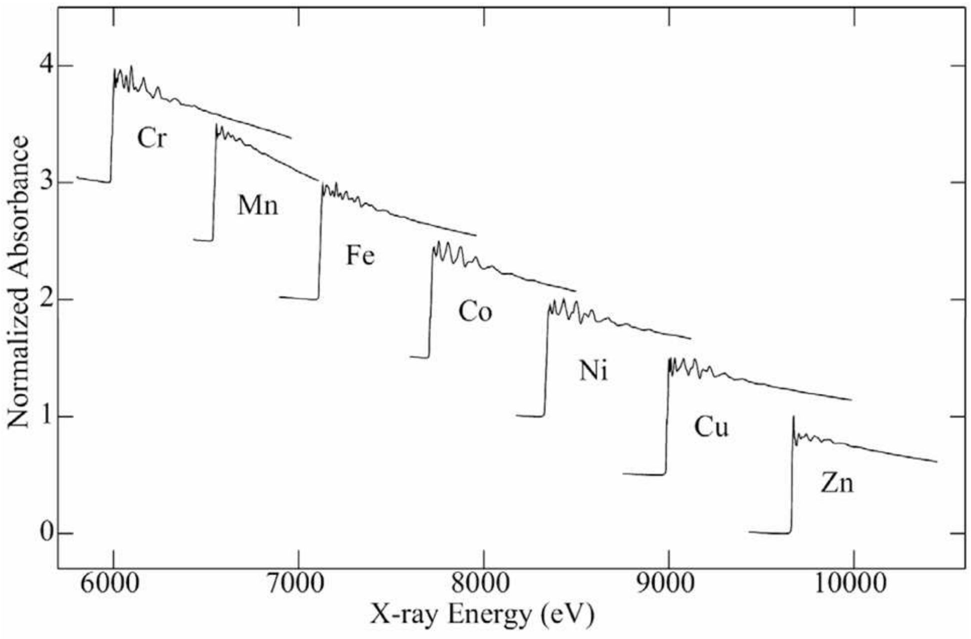

Fig. 2: *X-ray* K *-edge absorption of some* 3d *transition-metal foils. This figure clearly proofs the elemental selectivity of X-ray absorption. Above the edges the spectra clearly show some of the fine structure which is the subject of this contribution [23].*

---

[3] Here again we have a single particle picture. This time with a d hole ground state and a p hole excited state. In this picture the energy scale is turned upside down.

[4] Using the relationship (7) Dauvillier and Urbain in 1922 were able to identify element 72 (Hafnium) by its L emission lines [22]

Fig. 2 shows K-edge absorption spectra of the 3d metals Cr to Zn. It clearly demonstrates the shift of the absorption edge with atomic number. The figure also displays some of the fine structure that we want to discuss.
Once created, a core hole will rapidly decay either by X-ray fluorescence or by an Auger transition. Thereby the core hole is refilled by an electron from a higher level. In the first process a characteristic X-ray Photon is simultaneously emitted. As an optical transition it also obeys dipole selection rules. The photon energy matches the energy difference of the two levels and is characteristic to the atom. The emission lines are denoted by the signature of the initial core hole (K,L,M,...) with a numbered Greek index identifying the shell and the level from which the transition electron originates: K_{α_1,α_2}, K_{β_1}, ...
As an example Fig. 3 shows levels and transition lines for Cu (Z= 29). The position of the corresponding absorption edges which always are higher in energy are given as well [24, 25]. In the Auger process the excess energy is taken away by another electron [5]. Note that the Auger transition is not a two step process, but a single quantum mechanical transition. Auger transitions are characteristic to the atom as well. They are not restricted by dipole selection rules. Auger transitions are denoted by the three electronic levels involved, e.g. $K\,L_{2,3}\,M_{2,3}$, where the first letter labels the initial core hole. They are further classified as Coster-Kronig

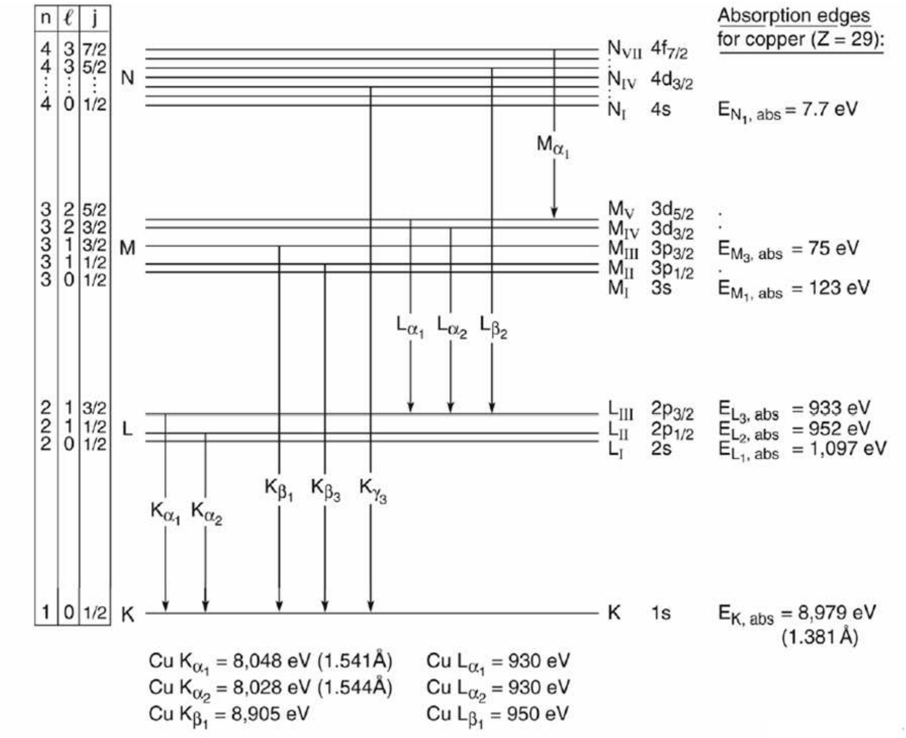

Fig. 3: *Correspondence of X-ray emission lines and participating atomic levels for the case of Cu (Z=29). The position of the absorption edges are also given [24, 25].*

---

[5] A review of the first 70 years of Auger spectroscopy has recently been given by W. Mehlhorn [26].

transitions, if one of the final-state holes has the same principle quantum number as the initial-state hole, e.g., $L_1 L_{2,3} M$, and super Coster-Kronig transitions, if both final-state holes have the same principle quantum number as the initial state hole, e.g. $L_1 L_{2,3} L_{2,3}$. Their energetics does not depend on the excitation process. This provides us with an easy means to distinguish Auger electrons from directly emitted photoelectrons. By changing the excitation wavelength the kinetic energy of direct photoelectrons will be shifted whereas the kinetic energies of Auger electrons are fixed. Such experiments can even be done at laboratory XPS - machines because usually two characteristic X-ray line sources are available, namely Al K_α at 1486.7 eV and Mg K_α at 1253.6 eV. The kinetic energy of the Auger electron can be estimated as $E_{kin} = E_{core} - E_1 - E_2$. Here E_{core}, E_1 , E_2 are the binding energies of the initial core hole and the other two electrons taking part in the process, respectively. Corrections will be necessary to this equation, however, because of correlation effects [27,28]. X-ray fluorescence and Auger transitions are competitive processes. Their relative abundance depends on the atomic number as shown in Fig.4. where the relative yield is plotted as a function of atomic number. For K -shell excitations the Auger transitions are dominant at $Z \leq 31$ (Ga) whereas the fluorescent emission is stronger at the heavier elements. For L-shell excitation the Auger transitions are dominant for all stable elements. Both processes, X-ray fluorescent emission and Auger decay themselves form the basis for widely used spectroscopies. Of course, Auger spectroscopy requires the better vacuum conditions. Due to the smaller scattering length of the ejected electrons it is also more surface

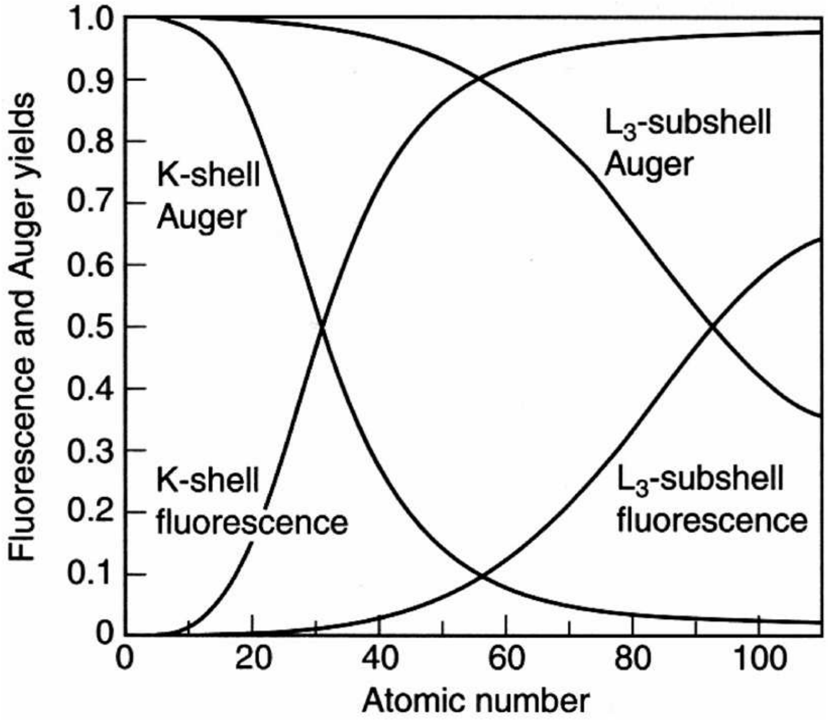

Fig. 4: *Comparison of X-ray fluorescence- and Auger yield as a function of atomic number for the* K *and* L_3 *absorption edges [25].*

sensitive than both, X-ray fluorescence spectroscopy and X-ray absorption spectroscopy.

For X-ray absorption the secondary processes imply the possibility of new detection schemes. An energetic Auger electron will often produce an avalanche of secondary electrons. A fraction of these will have enough energy to overcome the work function and leave the sample. Therefore, in the most easy experimental detection scheme the sample is simply connected to a pico-amperemeter and the drain current measured. This total-electron-yield (TEY) detection is a popular technique in solid state physics and surface science. The short scattering length of excited electrons limits the probing depth of this technique to about 10 nm. It is larger, though, than in XPS- and Auger measurements because here all the electrons are simultaneously collected, also the multiply scattered secondary ones. Alternatively, the emitted electrons and also the fluorescent photons may be measured by a suitable electron or photon detector in front of the sample. By choosing grazing incidence in reflection for the initial photon beam both detection techniques can be made surface sensitive. The distance that an electron can travel through the solid, the escape depth, varies with energy. Therefore, surface sensitivity can also be achieved by choosing only Auger electrons with a small escape depth for detection (partial-yield detection).

Fig. 5 shows a scheme of the experimental arrangement for a typical absorption measurement. In transmission mode a thin sample is placed into the monochromatized synchrotron beam. The beam intensity is monitored in front of and behind the sample by ionization chambers. It is common practice to measure the transmission of a reference sample in a third ionization chamber to eliminate fluctuations and to reliably detect small shifts of the samples absorption edge with respect to the reference. Fluorescence detection is preferentially used for very diluted absorbers because then the signal in transmission mode is the difference of two large intensities resulting in large background noise. Also the reabsorption of the fluorescence photons is minimized in this mode. Energy dispersive Si(Li)- detectors, szintillation counters or gas filled proportional counters may be used to discriminate the sample fluorescence from the background signal. Photodiodes, channeltrons and channel plates are also used for detection.

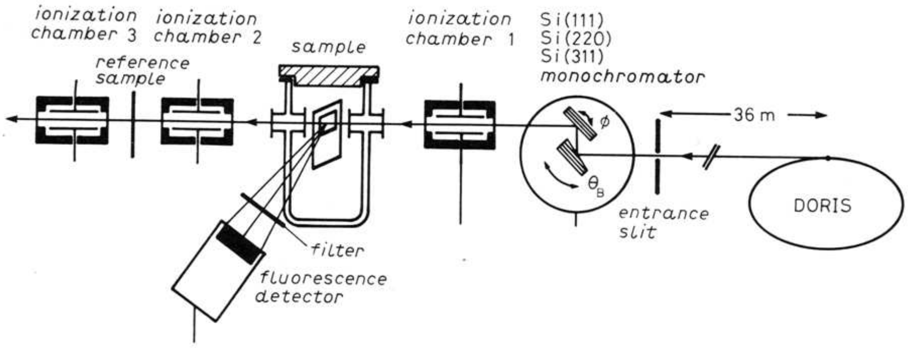

Fig. 5: *Arrangement of a typical X-ray absorption experiment[8,29].*

3 Near Edge and Pre-edge Structures

The XANES part starts at the first strong dipole allowed transition (s → p transition in case of a K-absorption edge) below the ionization limit. This is nicely demonstrated in the gas phase spectrum at the K absorption edge of Ne in Fig. 7.

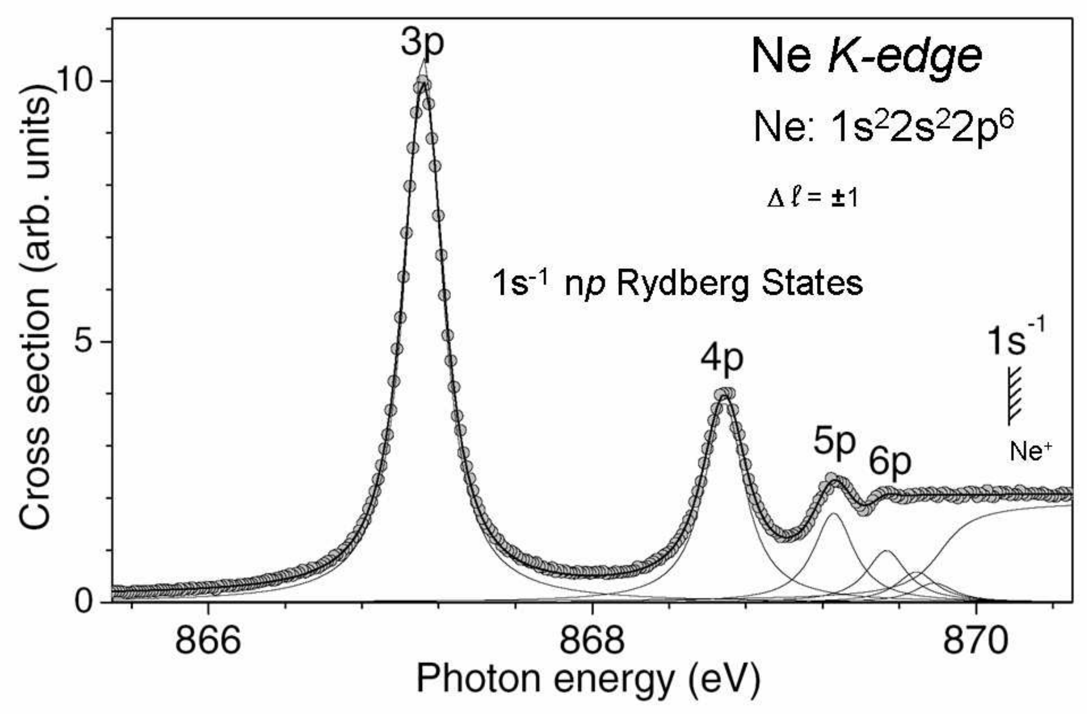

Fig. 7: *total cross section for photoionization of Ne in CO_2 at K edge absorption. The curves are fits to the data with a Gaussian with FWHM fixed to 66 meV [31].*

The Ne atom has a $1s^2 2s^2 2p^6$ configuration in its neutral ground state. Only transitions into unoccupied states are allowed. Therefore the first available unoccupied state in accordance with the $\Delta l = \pm 1$ selection rule is of 3p character, the next 4p, and so on. The ionization limit is also given. Note, that these levels correspond to $1s^{-1}np$ configurations where the negative exponent denotes the core hole. They do not give the positions of the atomic p levels but will be shifted due to correlation effects (screening).

The situation gets more complicated at the L-edges. Fig.8 shows the excitation at the L-edge of atomic Ar. Starting at the 2p levels the $\Delta l = \pm 1$ selection rule allows transitions to s and d levels. The first allowed transitions are to 4s and 3d. Due to the spin-orbit splitting of the 2p levels each peak appears twice. This is depicted in the level scheme on the right (but see also the discussion on the single particle picture above). The intensity ratio of corresponding levels is $\approx 2 : 1$ because the electron occupation of the 2p levels is 4:2 in favor of the $2p_{3/2}$ levels. Spectra like this are often used for monochromator calibration.

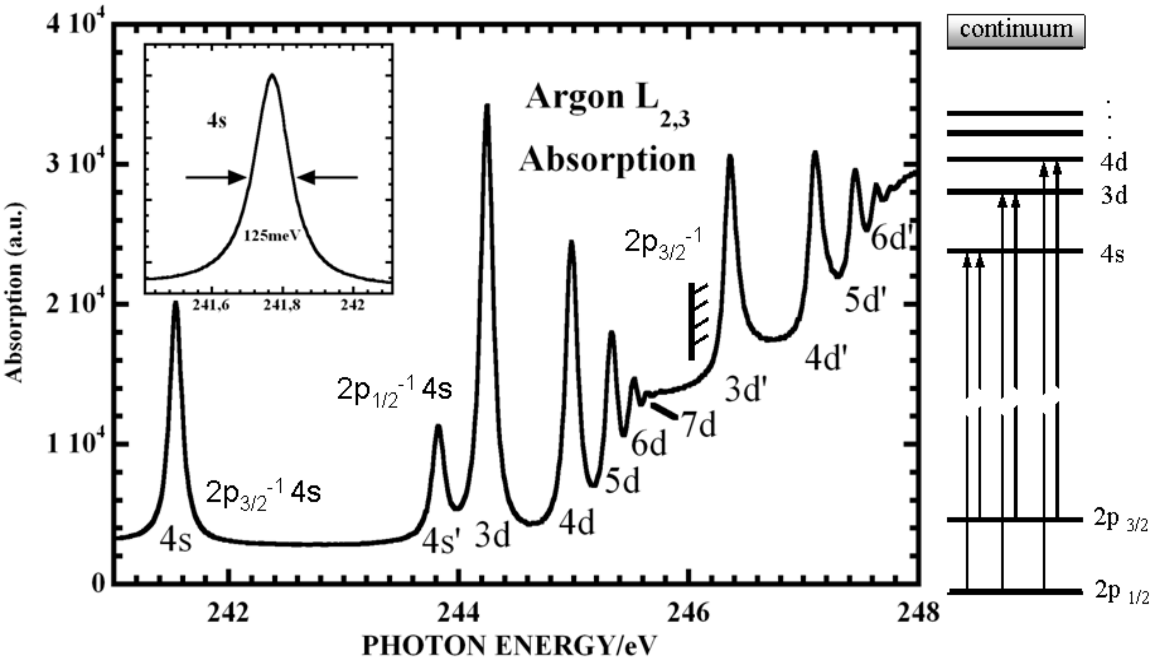

Fig. 8: *X-ray absorption spectrum of argon gas in the vicinity of the* $L_{2,3}$ *absorption edges and interpretation of the transitions in terms of the single particle picture. Such spectra are used to calibrate monochromators. [Courtesy of Stephan Cramm [1]]*

One might think that beyond the ionization limit of the 1s shell the X-ray absorption spectra of atoms will be smooth and flat as in Fig. 1. One rather observes multielectron excitations. These occur due to correlation effects. A typical example is a resonant double excitation process. The core electron is ejected by the photon and concomitantly a valence electron is excited to an empty valence orbital or ejected from the atom. In the first case we call it a “shake-up” process and in the second case a “shake-off” process. The shake- up and shake- off processes occur concurrently to the direct photoemission process. Of course, the total energy has to be conserved. Photoelectron waves passing through these two different pathways interfere with each other which results in an asymmetric line profile of the resonance in the photoabsorption cross section. They are called Fano resonances after U. Fano who predicted this lineshape [32]. One might see here a certain analogy to a double slit experiment. The electron has two optional pathways to go (this time on the energy scale) which leads to an interference pattern.

Fig.9 shows as an example 1s2s and 1s2p resonant double excitation spectra of Ne. The fit to the first peak shows a typical Fano profile [30, 31].

Fig.10 shows a high resolution K -shell absorption spectrum of N_2 in the gas phase. Above the ionization limit ($\approx$ 410 eV) besides the multi-electron excitations this shows a broad ”shape” resonance. Such resonances are absent for isolated atoms. They are attributed to quasi-bound states in the continuum in which photoelectrons with high angular momentum about the center of the molecule are trapped due to multiple reflections in a centrifugal barrier potential

$l(l+1)/2r^2$ which reaches into the continuum states. Since the energy and the width of the resonances depend on the shape of the potential, they are called shape resonances [37]. Multiple Scattering of the photoelectrons also happens in larger Molecules and solids. This and the occurrence of multi-electron excitations are the reasons why the XANES region is extended to about 30 eV beyond the absorption edge. In the EXAFS range a single scattering event is assumed (see below).

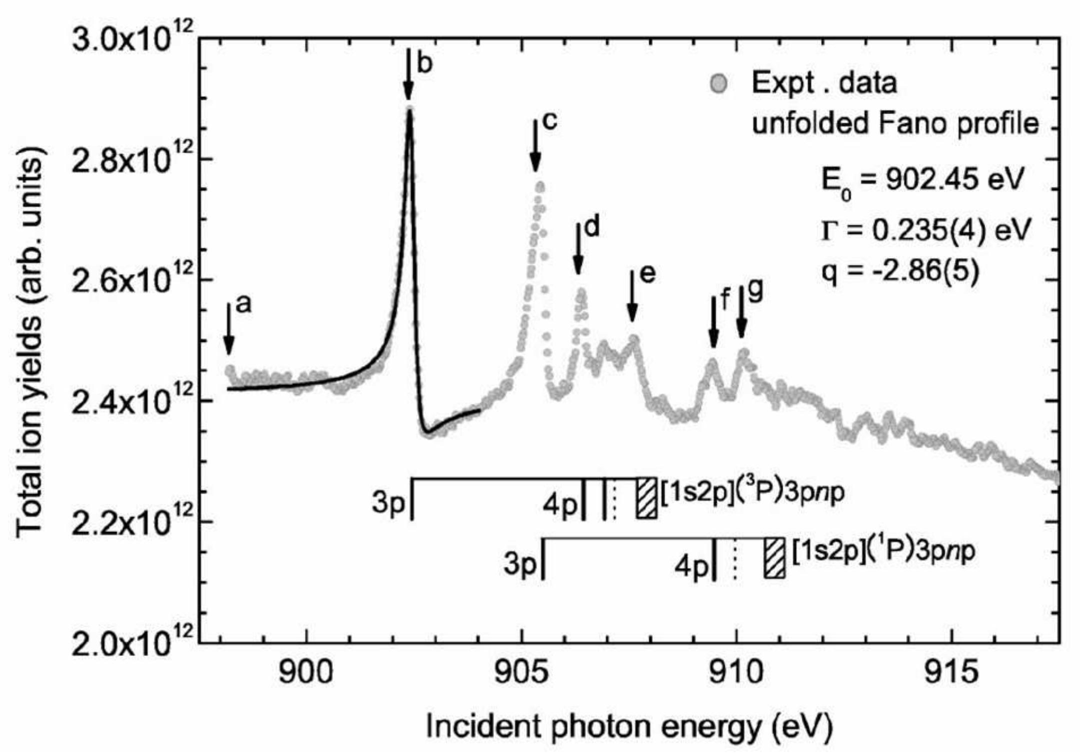

Fig. 9: *Double excitation spectrum of Ne with a Fano profile fit of the most intense line. The bars show the energies of the* $[1s2p](^{1,3}P)3pnp$ *series of transitions [33, 34].*

For compounds, XANES shows characteristic features for different coordinations of the absorber atom. Increasing the oxidation state of the absorber shifts the position of the absorption edge in the XANES to higher energies. This is demonstrated in Fig. 11 for some Manganese compounds [38].

The edge shifts linear with the valence state of the atom. This is qualitatively easy to understand: The radial distribution of the valence-electron charges contributes to the screening of the nuclear charge also in the vicinity of the nucleus. The transfer of valence electrons to the ligands reduces this screening. As a consequence the core electrons get less screened and stronger attracted to the nucleus and it will cost more energy to bring them to an excited state.

Some times one also observes peaks in the pre-edge region close to the onset of the absorption edge. These could be due to quadrupole transitions (s → d at the K or L_1 edge or p → f at the $L_{2,3}$ edges) to empty bound states. The selection rule for these to be allowed is $\Delta l = \pm 2$. However, quadrupole transitions are generally very weak in intensity. But, for transition metal compounds the pre-edge peaks are sometimes quite strong. They are then attributed to $p - d$ hybridization due to the interaction with ligands. In this case the transitions get dipole allowed due to orbital mixing.

Fig.12 shows as an example the K-edge absorption of oxygen coordinated chromium. First, we see the expected edge shift to higher energies when going from the 3+ to the 6+ valence state. The Cr^{3+} is 6-fold coordinated with an octahedral environment. With this coordination in the ideal octahedral geometry - one has a center of inversion and $p - d$ mixing is not allowed[6]

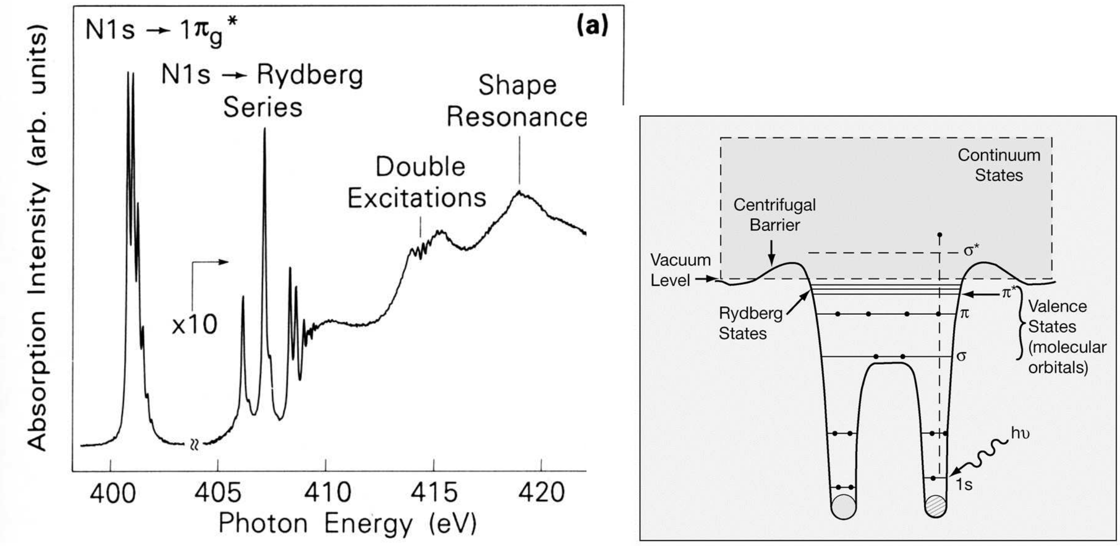

Fig. 10: *High resolution* K*-Shell photoabsortion spectrum of gaseous* N_2 *showing multi-electron excitations and a "shape resonance". The* $N1s \rightarrow \pi^*$ *resonance and the double excitation feature show vibrational fine structure. The Rydberg series merges in the ionization limit of* $\approx$ *410 eV [5, 35]. The figure on the right shows a scheme of a molecular potential including the centrifugal barrier (*$\propto l(l+1)/r^2$*) where here* l *is the angular momentum of the photoelectron with respect to the center of the molecule at* $\mathbf{r} = 0$*. This potential barrier temporarily prevents the photoelectron from leaving the molecule and gives rise to the* σ^* *shape resonance above the ionization limit [36].*

The small features observed in the pre-edge region are therefore either due to quadrupole transitions or due to a weak $p - d$ mixing induced by a slight distortion of the octahedron. The Cr^{6+} in the chromate anion ($[CrO_4]^{2-}$) is fourfold coordinated with a tetrahedral environment.

---

[6] Orbitals can mix only if they belong to the same irreducible representation of the molecular point group. p-orbitals are antisymmetric ("ungerade") with respect to inversion and d-orbitals are symmetric ("gerade"), respectively. Therefore they do not mix as soon as the point group contains a center of inversion.

Neutral Cr has a $[\mathrm{Ar}]3d^5 4s^1$ configuration. Thus, in its formal 6+ valence state the Cr has no d-electrons at all in its valence band. The strong $p - d$ hybridization in the tetrahedral geometry will therefore provide a large density of empty valence states for the transition [7]. This example shows that the pre-edge region can give valuable information not only on the valence state but also on the coordination of the absorber atom.

A similar pre-edge peak has recently been reported for Fe(VI)-oxide in solution and is also interpreted as $p - d$ hybridization with oxygen p-levels due to tetrahedral coordination. [40] The Fe(VI) has 8 empty d-orbitals and therefore also provides a high density of empty d-states which together with the hybridization also gives raise to a strong pre-edge peak.

According to Fermi's Golden Rule (eq. 6) the transition matrix element depends on the polarization of the X-rays. This can be exploited with anisotropic samples to determine bonding directions of the final state. The absorption cross section depends on molecular orientation. Therefore, XANES can be used to determine the orientation of molecules on surfaces [5, 41, 42].

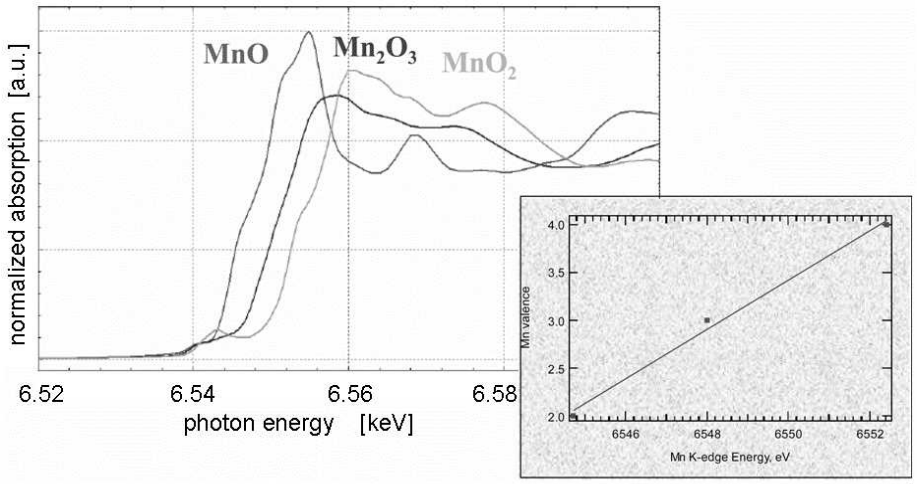

Fig. 11: *Shift of the Mn* K*-edge position for three different manganese oxides. As shown in the inset the position of the absorption edge for* Mn^{2+}, Mn^{3+}, *and* Mn^{4+} *compounds shifts linearly with the oxidation state of the absorber atom. This property can be used to identify the oxidation state of transition metal ions in unknown or complicated compounds like biomolecules [38].*

---

[7] Cr^{6+} compounds are very toxic. Therefore, this technique might help to identify them in critical cases.

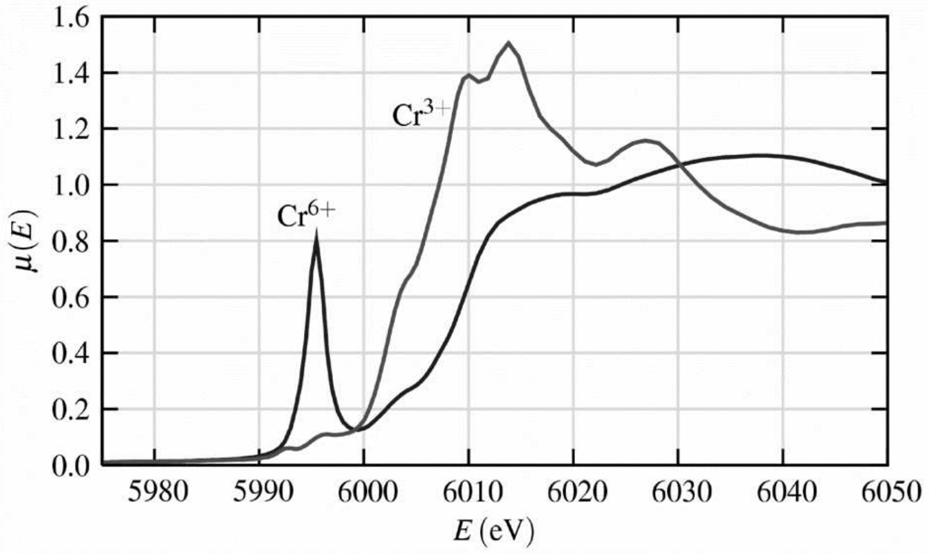

Fig. 12: *Cr K-edge XANES for Cr3+ and Cr6+ oxides. Here the strong pre-edge peak in the Cr6+ spectrum is a consequence of the tetrahedral symmetry causing considerable mixing of the empty d-electron orbitals with the p-states that the photo-electron will occupy [39].*

In conclusion, the XANES and the pre-edge structures tell us a lot about electronic structure. XANES is element specific, it probes the local unoccupied partial density of states in accordance with dipole selection rules. It is sensitive to the oxidation state and the coordination of the selected elemental species investigated and can be used to determine the orientation of adsorbate molecules. Difficulties arise, however, to interpret the spectral features in a quantitative way. This can easier be obtained with the EXAFS that we will discuss in the next chapter.

4 EXAFS (Extended X-ray Absorption Fine Structure)

About 30 eV beyond the absorption edge begins the EXAFS region [8,29,39,43-45]. In this range the photon energy is far above the ionization threshold and the photoelectron is treated as an outgoing spherical wave as schematically shown in Fig. 13.

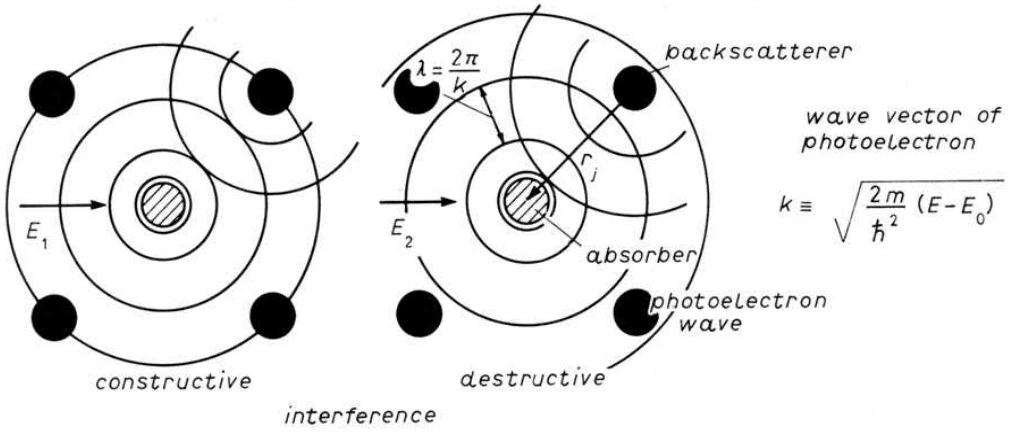

Fig. 13: *Scheme of the outgoing and backscattered electron wave leading to the EXAFS oscillations.* E *is the energy of the absorbed photon and* E_0 *the core level binding energy [8, 29].*

If there are other atoms surrounding the absorber atom they will scatter this wave. The outgoing wave and the scattered waves will interfere. The final state is the superposition of the outgoing and the scattered waves. For a constructive interference the signal will be enhanced leading to a maximum in the EXAFS oscillation. A destructive interference will lead to a minimum. The oscillations are absent in case of an isolated absorber atom. To quantify these ideas it is convenient to convert the energy scale into a wave number scale of the photoelectron. From the photoelectron's kinetic energy $E_{kin} = E - E_0 = p^2/2m = (\hbar k)^2/2m$ we get

$$k = \sqrt{\frac{2m}{\hbar^2}(E - E_0)} \tag{8}$$

where E is the energy of the absorbed photon and E_0 is the energy of the ionization threshold. Then, using a plain wave approximation at the scattering atoms and allowing only for a single scattering event one can derive the following equation for the EXAFS oscillations [29,39,43]:

$$\chi(k) \equiv [\mu(E) - \mu_0(E)]/\mu_0(E) = \sum_j N_j F_j(k) D_j(k) e^{-2\sigma_j k^2} \frac{\sin\left(2kr_j + \phi_j(k)\right)}{kr_j^2} \tag{9}$$

Here $\mu_0(E)$ is the signal of the isolated absorber atom, which has been subtracted from the measured signal and to which the EXAFS oscillations are normalized. Of course, this function is not known but can be approximated by an extrapolation e.g. of the Victoreen function below and above the absorption edge [8]. The EXAFS oscillations are summed over all neighboring shells $\mathbf{j}$ of scatterers which are separated from the absorber by the same distance $\mathbf{r}_j$. N_j is the number of scatterers in one shell. The periodicity of the oscillations is determined by the sin function, where $2\mathbf{r}_j$ is the double distance between the absorber and a scatterer and φ_j is the total phase shift of one round trip of the wave. $F_j(k)$ is the backscattering amplitude of the neighboring atoms. The exponential is a Debye-Waller factor which describes the damping of the wave due to statistical disorder of the atoms and due to thermal motion [99]. Inelastic scattering of the photoelectron destroys its coherence. This is taken care of by the additional damping factor $D_j\ (k) = e^{-2r_j\ /\Lambda}$ where $\Lambda(k)$ is the mean free path of a photoelectron. The EXAFS formula has been derived under some simplifying assumptions: The photoelectron is treated as a plane wave at the positions of the neighbors. Multiple scattering contributions are not contained. These are largest for small k-values and for collinear arrangements of 3 atoms in a row. Moreover, the energy E_0 is not well defined. Therefore the EXAFS is often compared to a well characterized model compound from which better parameters can be deduced. Thereby it is hoped that the parameters are identical and that the uncertainties will cancel out. For larger k values respective shorter wavelength the dephasing increases and the oscillations will die away. Today computer codes are available which take corrections due to the curvature of the photoelectron wave as well as multiple scattering events into account.

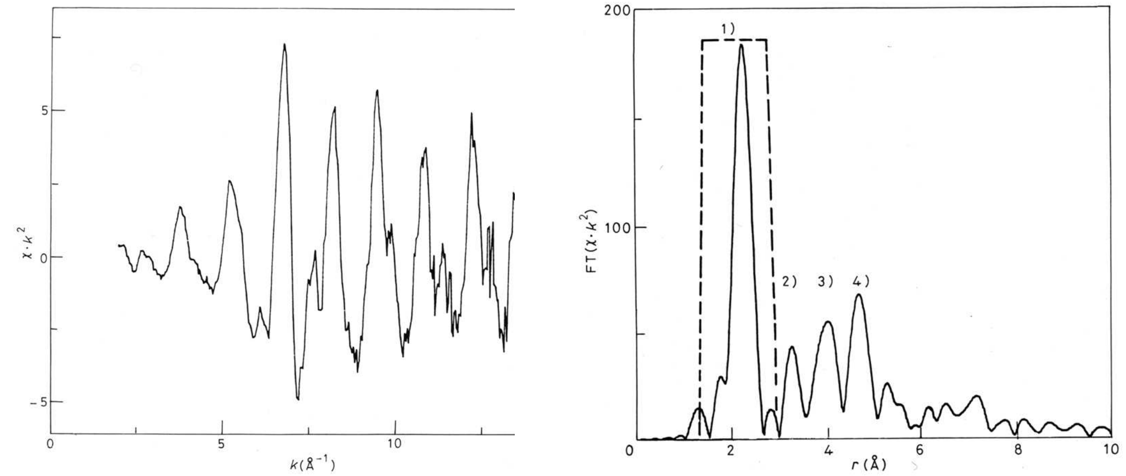

Fig. 14: *(a)* k^2 *weighted EXAFS* $\chi \cdot k^2$ *at the Ti* K *edge of a diluted NiTi alloy containing 2% Ti. The measurements were made at 77 K. (b) Fourier transform of the EXAFS. Four shells of neighbours can be identified. The first shell peak is covered by a filter function.*

---

[8] there are other ways to handle this [29,39]

[9] to reduce the latter effect it is advantageous to measure at low temperatures.

Fig. 14 shows as an example the EXAFS oscillations at the Ti K edge of a diluted NiTi alloy with 2 at. % Ti, measured at 77 K. Since the oscillations decay quickly they have been weighted by k^2. These oscillations are represented in k-space. To get real space information, that is to derive interatomic distances, we have to fourier transform the data. This is done in Fig. 14b. One clearly sees displayed the radii of the first four Ni coordination shells around a Ti atom. It is found that the 12 nearest neighbours are shifted outwards by (0.022 ± 0.005)Å. The atoms in the other coordination shells are at the Ni lattice sites.

In summary, the EXAFS is a superposition of sinusoidal waves that decay in intensity as the incident energy increases from the absorption edge. The sine waves result from the interaction of the ejected photoelectron wave with the surrounding atoms. The amplitude and phase depend on the local structure in the neighborhood of the excited atom. This structure is determined by fitting a theoretical spectrum to the experimental data. The procedure yields information on the distance of neighboring atoms, their identity, and number, and by the Debye-Waller factor the degree of disorder in the particular atomic shell.

5 XMCD: X-ray Magnetic Circular Dichroism

Dichroism denotes the property of anisotropic materials to change color when irradiated with light in different directions and/or of different polarization. It is associated with direction- and polarization- dependent differences in optical absorption and with this understanding can be extended to other spectral ranges, particularly X-rays. Circular dichroism refers to absorption differences for left and right circularly polarized light, respectively [10] , and if induced by the presence of a magnetization we speak of magnetic circular dichroism.

XMCD can be observed with ferro- and ferrimagnetic systems [11]. It was first observed at the K-edge of iron [46]. Yet, much stronger signals can be observed at the transition metal $L_{2,3}$ edges of 3d transition metals. These are of particular interest because the d-electrons are the primary carriers of the magnetism. Therefore, in this introduction the discussion will be limited to these cases.

Fig. 15a shows the absorption-cross sections at the $L_{2,3}$-edges of Fe, Co, Ni and Cu films [47]. The strong absorption peaks at the edges are often referred to as the “white lines” [12]. Their intensities decrease with increasing occupation of the d levels. For copper they are nearly absent, due to its almost completely filled d shell. To extract from these spectra the pure p → d transition intensity a two step background (due to transitions p → s, p-derived delocalized band states) is subtracted as indicated in the spectrum of iron. The step function for the L_3 edge is twice as high as the one for the L_2 edge because of the different occupation numbers of the $2p_{3/2}$ and $2p_{1/2}$ levels, namely 4 and 2, respectively.

After background subtraction the integrated white-line intensities reflect the number of holes in the d band (Fig. 15b) [47-49]:

$$I(L_3) + I(L_2) = Cn_h = C(10 - n) \qquad (10)$$

where n_h is the number of d holes in the electronic ground state and n is the number of occupied d states. This rule is called the ”charge sum rule”. Here, and in the following we will assume that anisotropies caused by anisotropic charge and spin distributions in the crystallographic unit cells

---

[10] For circularly polarized X- rays the electric field vector rotates about the direction of propagation. According to the classical definition of circular polarization the wave is called right circularly polarized if the light vector turns to the right for an observer looking into the beam and left circularly polarized if the light vector turns left. However, in X-ray spectroscopy not all investigators cling to this definition. Therefore it might be more adequate to refer to the light helicity which is positive if the photon angular momentum points into the propagation direction of the light (σ^+ light; left circularly polarized according to the above rule)) and negative, respectively, if the photon angular momentum points in the opposite direction (σ^- light). X-ray natural circular dichroism (XNCD) has been observed in the uniaxial gyrotropic single crystal $LiIO_3$. [50]

[11] It has also been studied with paramagnetic samples. This requires low temperatures and strong magnetic fields of several Tesla. Here the net spin orientation is obtained by the Zeeman interaction. Some applications to bio-inorganic molecules and molecular magnets are summarized by Funk et al. [51]. We will not discuss this any further.

[12] This nomenclature stems from the early days of X-ray spectroscopy when the absorption was still measured with photographic films. The films were not exposed at the position of the strong absorption lines and therefore appeared to be white.

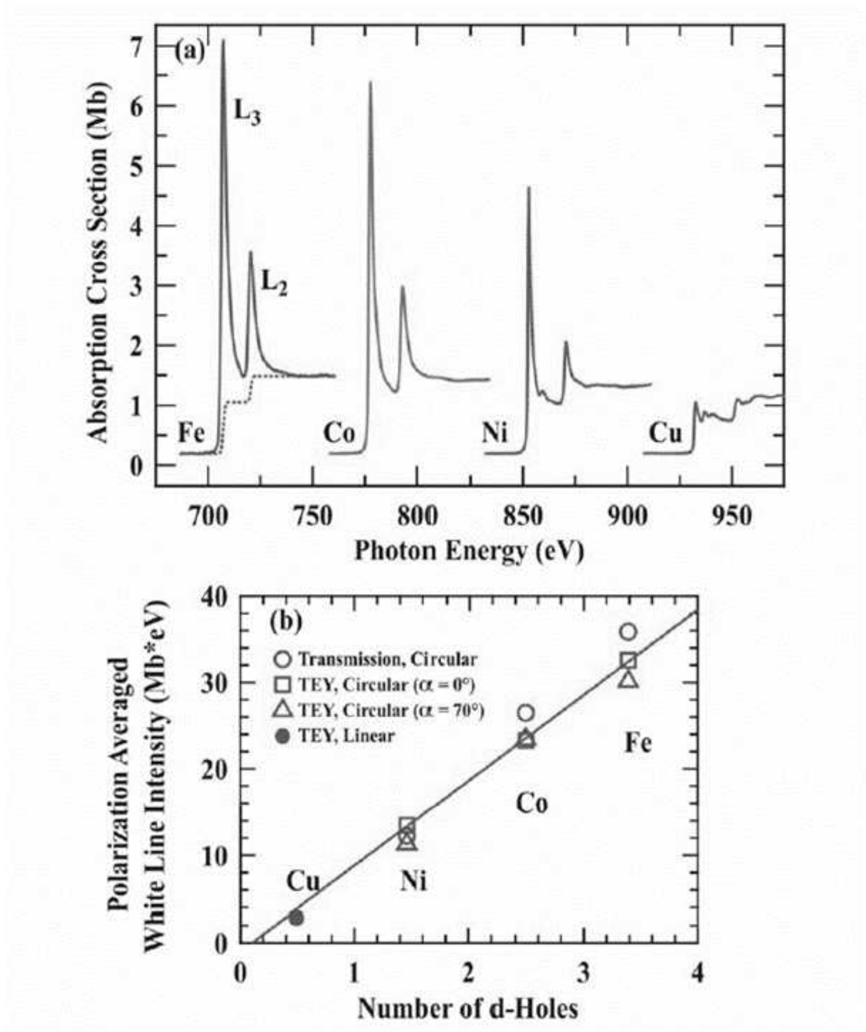

Fig. 15: *L edge X-ray absorption spectra for Fe, Co, Ni, and Cu metal. (b) White-line intensity, determined after subtraction of a double step function [52], shown dashed in the Fe spectrum in (a), versus calculated number of* d *holes [47].*

are averaged out. Experimentally this can be achieved by averaging over three measurements performed in three orthogonal directions [49]. In a tight binding approximation the constant C is calculated to be: $C = \frac{2}{15} A\mathfrak{R}$ where $A = 4\pi^2 n\omega\alpha_f$ and $\mathfrak{R}$ is the radial transition matrix element [49, cf. appendix].

$\hbar\omega$ is the photon energy and $\alpha_f = \frac{e^2}{4\pi\varepsilon_0\hbar c} \approx \frac{1}{137}$ is Sommerfeld's fine structure constant.

Thus XAS probes the unoccupied density of states (DOS) above the Fermi level.
If, in addition to relation (10), we could distinguish between spin-up and spin-down DOS we were able to measure the magnetic moments of the samples with element selectivity on an atomic level. Therefor the excitation of core electrons has to be spin selective. This can

indeed be achieved by using circularly polarized light. It requires the presence of two basic inter- actions, namely spin-orbit coupling and an exchange splitting of the electronic valence states. With the aid of Fig. 16 we will explain the role of the spin-orbit coupling. In Fig. 16 we study the transitions from 2p initial states to 3d states when we excite the 2p- states with σ^+ light. The transitions are energetically separated by spin-orbit interaction.

The states can be described as linear combinations of $|m_l, m_s>$ kets and it is sufficient to study transitions between those. Transitions from the $2p_{\frac{3}{2}}$ and $2p_{\frac{1}{2}}$ initial states are treated separately.

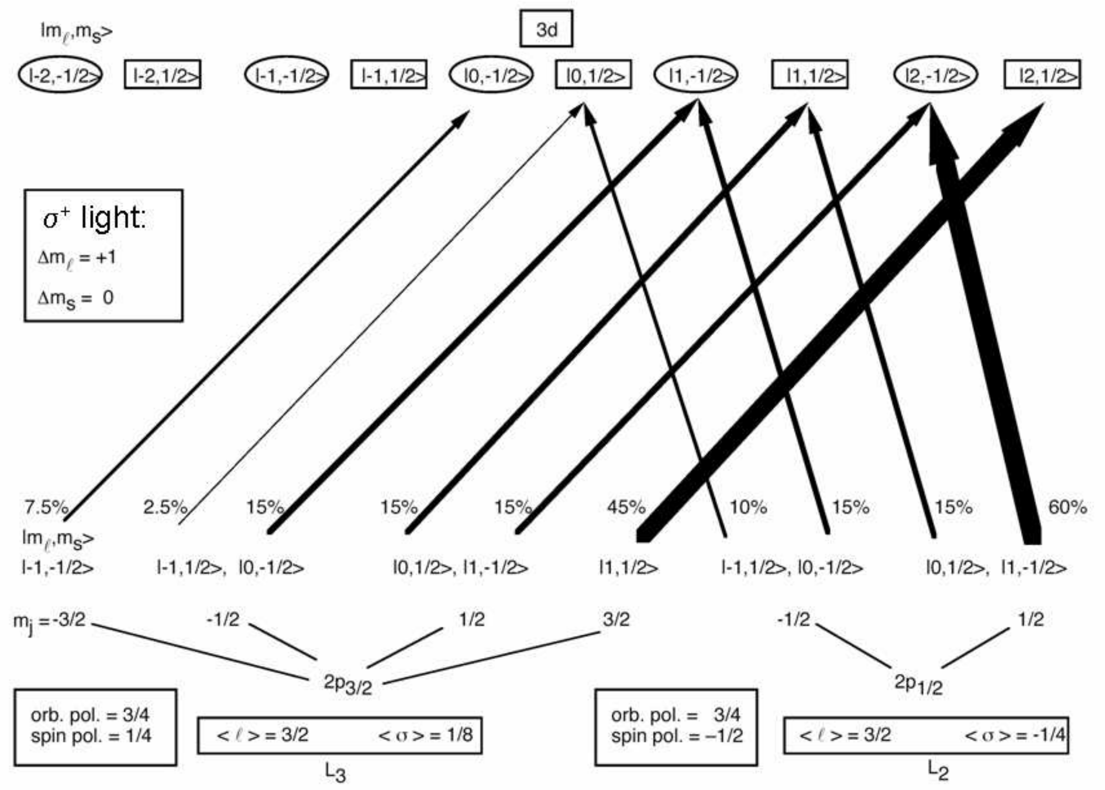

Fig. 16: *Scheme of possible* 2p → 3d *transitions when excited with* σ^+ *light [53]. The upper row shows the ten* 3d *final state levels sorted by their* m_l *and* m_s *quantum numbers. Spin-orbit splitting is neglected for the* 3d *states. They are labeled by rectangles (positive* m_s *) and ellipses (negative* m_s *). It is assumed that all* d *levels are unoccupied prior to the transition (there are no restrictions due to the Pauli-exclusion principle). Below, the spin-orbit split 2p levels are given. The magnetic sublevels are indexed by their magnetic quantum number* m_j *. The upper line shows uncoupled* m_l, m_s *states that contribute to the respective* m_j *states according to the Clebsch-Gordon series (see appendix). Allowed transitions - represented by arrows - must obey dipole selection rules (for* σ^+ *light:* $\Delta m_s = 0$ *and* $\Delta m_l = +1$*). The line thickness corresponds to the transition strength. Separately for each spin-orbit split component the transition strength is also given in % as calculated in the appendix. For the* $2p_{\frac{1}{2}}$ *level 75 %are spin down transitions and 25 % spin up. This results in a net spin polarization of* $\frac{-75+25}{75+25} = -\frac{1}{2} = -50\%$

The spin-orbit splitting of the d states, which is much smaller than that of the 2p states is neglected. For σ^+ light the transitions have to obey the dipole selection rules with $\Delta m_l = +1$ and $\Delta m_s = 0$. Here it is assumed that all the d-states are unoccupied and can be reached (no restrictions due to the Pauli principle). The width of the arrows corresponds to the calculated transition probabilities (In the appendix it is shown how this result is derived from calculations of transition matrix elements). The transition strengths are also given in %. If for the $2p_{1/2}$ initial state we add all the transitions with identical spin we find a total probability of 75 % for a transition with $m_s = -1/2$ (spin down) while transitions with $m_s = +1/2$ (spin up) contribute only 25 %. As a result we end up with a spin polarization of 50 % (spin down) in the final d-states if only $2p_{1/2}$ states are excited. The spin expectation value is then $\langle\sigma\rangle = -1/4$.[13] Similarly, if only $2p_{3/2}$ initial states are excited we get 37.5 % spin down and 62.5 % spin up electrons in the excited states. This results in a net spin polarization of 25 % (spin up) electrons and a spin expectation value $\langle\sigma\rangle = -1/8$. Note, that the spin polarization is opposite in the two cases. Since we have twice as many $2p_{3/2}$ states as $2p_{1/2}$ states the absorption strength of the $2p_{3/2}$ states is also doubled. Thus, if there is no spin-orbit splitting and all the states are excited simultaneously the net spin polarization in the excited state will be zero, as expected. One also observes an orbital polarization in the excited states. The orbital polarization is 75 % for both excitation pathways where $m_l = 2$ is fully polarized, $m_l = 1$ half-polarized and $m_l = 0$ non-polarized. When the polarization of the exciting photon is reversed ($\sigma-$ light), the polarization of the excited electrons is reversed as well. Thus, if the d states are unoccupied there is no difference in the absorption for both circular polarization directions of the light. The same is true if the d-states are partially occupied with electrons but the same number of electron spins points towards the beam as in the opposite direction.

The amazing fact, that spin polarized electrons can be generated by photoexcitation of unpolarized atoms with circularly polarized light if the states can be separated by spin-orbit splitting was predicted by U. Fano in 1969 [54]. The effect is therefore called Fano effect.[14] It is now widely used to generate spinpolarized electrons from GaAs sources [55-58].

Above, it was stated that, besides spin-orbit coupling, we need exchange interaction to observe the circular dichroism. In the valence band of a ferromagnet (as well as in a ferrimagnet) the exchange interaction leads to different densities of states for majority and minority spins, $\rho\uparrow$ and $\rho\downarrow$. Then there are different numbers of d holes available for σ^+ and σ^- light. This destroys the absorption symmetry. The XMCD signal is just the difference of the absorption for these two cases.

Fig. 17 (left) shows the magnetic circular dichroism spectrum of an ultra thin Co film on Cu(001)[53,60,61]. In the upper panel, the absorption spectra in the photon energy range of the Co 2p → 3d transitions are shown for σ^+ and σ^- light. For a fixed sample magnetization the absorption at the L_3 peak (corresponding to $2p_{3/2} \rightarrow 3d$ transitions) is higher for σ^+ polarization (continuous line) compared to $\sigma-$ polarization (dashed line), while the situation is opposite at the L_2 peak ($2p_{1/2} \rightarrow 3d$ transitions). The bottom panel displays the dichroism

---

[13] Note, that $\langle\sigma\rangle = 1/2$ means 100 % down spin polarization.

[14] not to be mixed-up with the earlier mentioned Fano resonance.

spectrum, which shows different sign at the two Co absorption edges. The signal scales as the inner product q · M where q is the propagation direction of the circularly polarized photons and M is the sample magnetization[15].

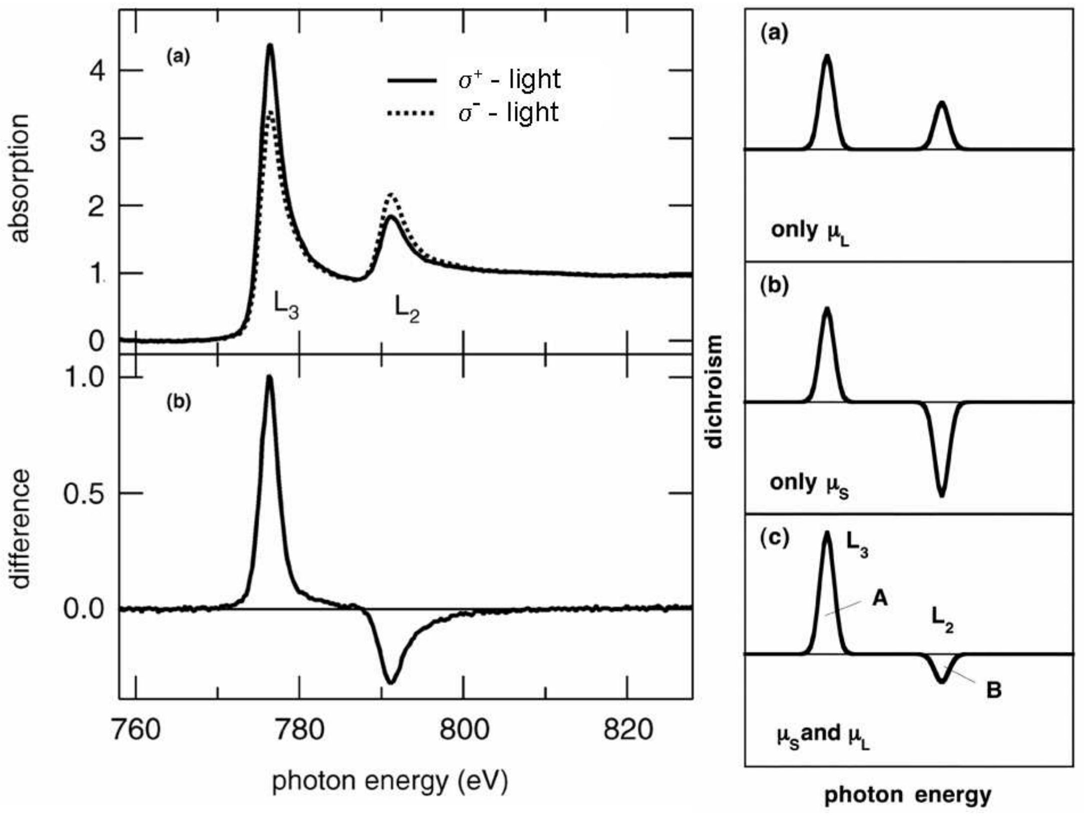

Fig. 17: *Left: XMCD spectrum of a thin Co film on Cu(001). (a): Absorption spectra at the Co* $L_{2,3}$ *edges for* σ^+ *(continuous line) and* σ^- *polarization (dotted line) of the exciting X-rays. The magnetic dichroism is visible as a difference in the absorption strength.(b): Difference of the two spectra (XMCD spectrum). The sign of the dichroism is opposite at the* L_3 *and* L_2 *edges. This is due to the inverse spin polarization of the* $2p_{3/2} \rightarrow 3d$ *and* $2p_{1/2} \rightarrow 3d$ *transitions. Right: Scheme to illustrate the separate orbital and spin contributions to the XMCD spectrum. (a) hypothetical XMCD spectrum obtained from orbital magnetic moments alone, (b) hypothetical spectrum with contributions of the spin magnetic moments alone, (c) XMCD difference spectrum of a sample with both spin and orbital magnetic moments. [60,61].*

In the appendix we have shown how within a simple model we can calculate the XMCD signal starting from a magnetic ground state with a given d orbital occupation. This procedure can principally be inverted. Important sum rules have been derived to extract from the experimental

---

[15] This rule holds for absorption and total yield measurements. Deviations may occur when partial yield detection is used [62]. Therefore, with electron detection modes special care has to be taken.

spectra the ground state expectation values of the orbital and spin angular momenta, separately [63-68, see also 48,49,52,69]. The "orbital sum rule" [63,65,66] relates the average orbital moment per atom with the peak intensities according to

$$\mu_l = -\frac{2}{3C}(A+B)\mu_B$$

The constant C is the same as the one for the charge sum rule given above (10). The notation for the A and B is given in fig.17 (right panel). Correspondingly, the "spin sum rule" [64] links the dichroism intensities with the size of the spin moment per atom according to

$$\mu_s = -\frac{1}{C}(A-2B)\mu_B$$

Note, that the area of B is negative. Therefore in the derivation of μ_l the difference of the two areas has to be taken, which will lead to a considerable error when both areas come close to each other.

To make the sum rules plausible we follow the line drawn by Kuch [60,61] (Fig 17 right panel). From Fig. 16 and the calculation given in the appendix we know that the orbital contribution to the $2p_{3/2} \rightarrow 3d$ transition is twice that of the $2p_{1/2} \rightarrow 3d$ transition. Upon reversal of the light helicity from σ^+ to σ^- spin and orbital polarizations will both change sign, i.e. in a difference spectrum they will both add in the same sense. Thus a hypothetical spectrum with only orbital admixture would give a spectrum as plotted in Fig. 17(a)(right panel) where peak A has the double size of peak B. If, on the other hand, we consider a spectrum with only spin contribution the peaks A and B have opposite sign as shown in the middle part of the figure. The higher spin polarization of transitions at the L_2 edge compensates the lower electron occupation of the $2p_{1/2}$ level leading to opposite peaks of equal size. This is also in agreement with our calculation and Fig. 16. A realistic spectrum with both, spin and orbital contributions, would be a linear combination of these two (Fig 17(c)). Now we see, that addition of peaks A and B will eliminate the spin part and retain the orbital part only. If we take $(A-2B)$ we will eliminate the orbital part and retain only the spin part. A more rigorous calculation gives the results reported in the sum rules above.

So far, it was assumed that anisotropies are averaged out. This is acceptable for bulk transition metals. More general forms of the sum rules are discussed elsewhere [48,52,69,70]. Particularly, for thin films the spin magnetic moment has to be supplemented by a magnetic dipole term which can be of the same order of magnitude as the orbital magnetic moment.

The sum rules are derived under some simplifying assumptions. For instance the electronic transitions are considered to take place between states of free atoms. Many particle effects are neglected. Nevertheless they are considered to be correct within $\approx \pm 10$ %. The reader is refered to refs. [48,49,52,69,70] for more detailed discussions. A very readable article with a user friendly discussion of the general sum rules is given in [69].

It is one of the major achievements of XMCD that it gives experimental access not only to the spin magnetic moment but also to the orbital magnetic moment which is closely related to the magnetic anisotropy energy [71]. The orbital moment is small in solids but its contribution to the total magnetic moment/atom increases as the sample dimensions become smaller from thin films to nanowires to clusters [72-79].

One of the major applications of XMCD today is the study of magnetic domains on a microscopic level in a photoelectron emission microscope (PEEM). Due to its element selectivity and its relatively large penetration depths it offers the unique possibility not only to study the magnetic structure of multilayers layer by layer but also the coupling between layers that are separated by nonmagnetic spacer layers. Such structures are of great technological importance in todays magnetic storage devices and for spintronic applications [16].

6 XMLD: X-ray Magnetic Linear Dichroism

Besides the XMCD there exists a magnetic linear dichroism, which can be observed with linearly polarized X-rays with the polarization direction aligned parallel and perpendicular to the magnetic field, respectively [80,81].

The application of a magnetic field to a medium (internally or externally) breaks its symmetry. According to Curie's principle [82] [16] the medium gets uniaxially distorted, e.g. a cubic crystal exposed to a magnetic field will show a uniaxial symmetry. This can be probed by linearly polarized light and will be invariant with respect to a reversal of the magnetic field. The anisotropy will therefore scale as (M^2) to first order [80]. The largest anisotropy will occur when the propagation direction of the light is perpendicular to the magnetic field and the polarization direction is changed from parallel to the magnetic field to perpendicular. This is the basis of XMLD. It is one of the major advances of XMLD that can be applied to antiferromagnetic materials as well. Such materials are used in magneto-electronics to pin the magnetization of ferromagnetic layers by an exchange biasing interaction.

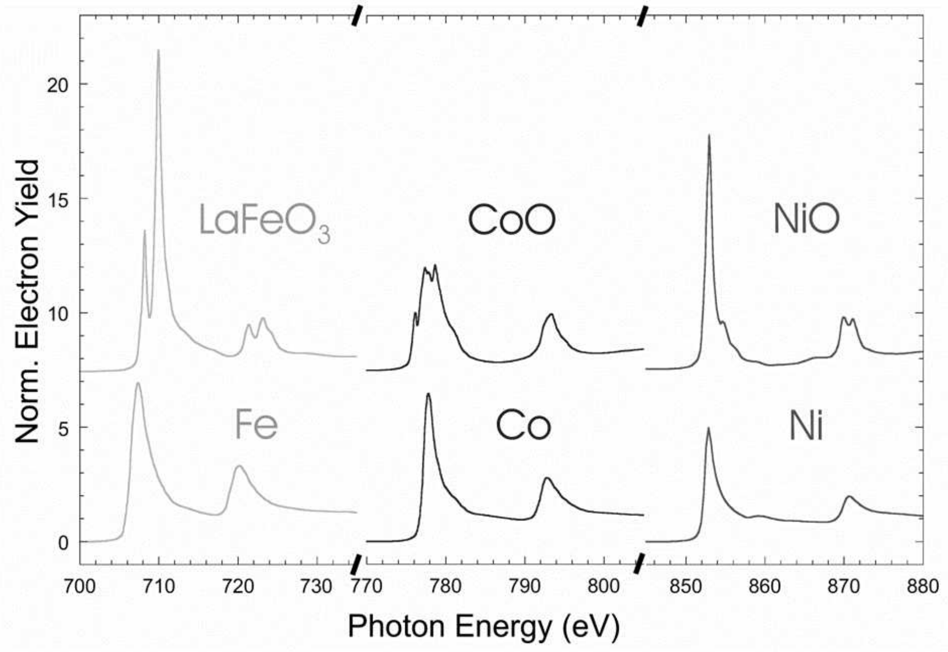

Fig. 18: *L edge X-ray absorption spectra for Fe, Co, Ni, compared to those of some antiferromagnetic oxides.* 2p *core electrons are excited to empty* d *states in all the spectra. The oxide spectra show more detailed fine structure due to multiplet splitting and crystal field effects [84].*

Fig. 18 compares X-ray absorption spectra of Fe, Co, and Ni with those of some antiferro-

---

[16] The Curie principle states that the symmetry group of the system with an influence (here the magnetic field) G_m contains a common subgroup of the symmetry group of the system without this influence G_s and the symmetry group of the influence G_i alone: $G_m \supseteq G_s \cap G_i$.

magnetic oxides. The spectra of the antiferromagnets have a richer structure which cannot be interpreted in terms of a simple single particle picture. The structures occur due to multiplet splitting and crystal field effects [83]. Fig. 19 demonstrates the XMLD at the L_2 edge of a NiO (100) thin film when the light polarization is changed from parallel to the magnetic field (solid line) to perpendicular (dashed line).

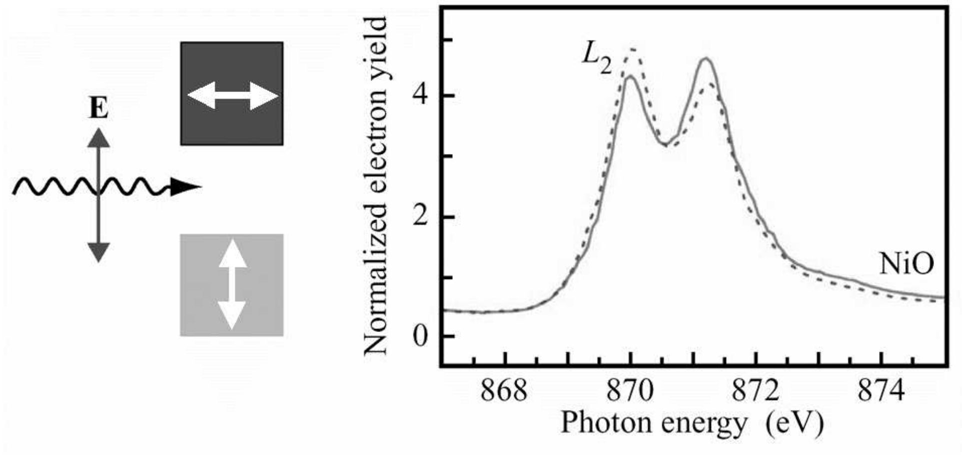

Fig. 19: *XMLD spectrum of a NiO film at the* L_2 *edge. The spectrum was recorded by electron yield detection for 45 nm thick NiO (100) film grown on MgO (100). The polarization of the X-rays was changed from parallel to the magnetic film (solid line) to perpendicular (dashed line) [85,86].*

In NiO successive (111) lattice planes have opposite spin alignment. Thus ”uncompensated” surfaces can be generated at the surface of a single crystal. Within the surface the magnetic moment has three equivalent possibilities to orient, namely in $[\bar{2}11]$, $[1\bar{2}1]$ or $[11\bar{2}]$ directions. Together with the four equivalent (111) surfaces this results in 12 possible spin orientations, and, thus in 12 different possibilities to form antiferromagnetic domains. To proof that the anisotropy is due to the antiferromagnetic alignment and not due to another anisotropic effect one can heat the sample to its Neél temperature (520 K for NiO) where the magnetic contribution will disappear.

XMLD can also be used for domain imaging by means of photoemission electron microscopy, PEEM [16]. This is of coarse particularly useful for antiferromagnets.

7 Conclusion

X-ray absortion spectroscopy is a local element-specific probe of the electronic and geometric structure of materials. It can likewise be applied to ordered and disordered samples. It can be used to study subsurface structures and does not rely on UHV conditions. The latter is particularly useful for catalytic interfaces and biological samples. At grazing incidence X-ray absorption gets surface sensitive with probe depths of 2-5 nm. In the XANES (NEXAFS) range it probes the projected electronic density of empty states (local partial density of States LPDOS) and the valence of absorber atoms. EXAFS probes the coordination number and the interatomic distance.

X-ray absorption spectroscopy probes transitions between core levels and empty valence states. It is not only element specific but also sensitive to the chemical environment. It is particularly useful for investigations of magnetic properties. XMCD measures the size of the magnetization per atom and its angle relative to the circular x-ray polarization vector. Sum rules exist for the number of d holes, the spin and the orbital moment. XMCD is used for the study of ferromagnets. XMLD measures the magnetic moment and the angle between the spin axis and the linear x-ray polarization vector. XMLD is used for the study of ferro- and antiferromagnets. In connection with photoemission electron microscopy (PEEM) X-ray absorption allows to visualize magnetic domains with a resolution of better than 100 nm. Dynamical processes can as well be studied. In connection with the free electron laser it will become possible to study transient electronic and dynamic processes on a femtosecond time scale.

8 Appendix

To obtain the transition rates in Fig.16 we have to evaluate the transition matrix element in Fermi's golden rule (equ.(6)). The following approach was first used by J. L. Erskine and E. A. Stern [87, see also:19,49,59,69]. For circularly polarized light propagating in the positive z-direction the normalized polarization vector for positive and negative helicity of the electric field is

$$\epsilon^{\pm} = \frac{e_x \pm i e_y}{\sqrt{2}}$$

where e_x and e_y are unit vectors pointing in the direction of the coordinate axes. The position vector is:

$$\mathbf{r} = \mathrm{x}\mathrm{e}_\mathrm{x} + \mathrm{y}\mathrm{e}_\mathrm{y} + \mathrm{z}\mathrm{e}_\mathrm{z}\,.$$

Thus, the polarization-dependent dipolar operator is given as:

$$\epsilon^{\pm} \cdot r = \frac{x \pm iy}{\sqrt{2}}$$

Introducing spherical harmonics

$$Y_{1,0} = \sqrt{\frac{3}{4\pi}\frac{z}{r}} = \sqrt{\frac{3}{4\pi}}\cos\theta \quad and \quad Y_{1,\pm 1} = \sqrt{\frac{3}{8\pi}}\frac{x \pm iy}{r} = \sqrt{\frac{3}{8\pi}}\sin\theta\, e^{\pm i\varphi}$$

where (r, θ,) are spherical coordinates. With:

$$x = r\sin\theta\cos\varphi = -\sqrt{2\pi/3}\,r\left(Y_{1,1} - Y_{1,-1}\right); \quad y = r\sin\theta\sin\varphi = i\sqrt{2\pi/3}\,r\left(Y_{1,1} + Y_{1,-1}\right)$$

$$z = r\cos\theta = \sqrt{4\pi/3}\,rY_{1,0}$$

we get the polarization dependent dipolar operator:

$$\epsilon^{\pm} \cdot r = \frac{x \pm iy}{\sqrt{2}} = \mp r\sqrt{\frac{4\pi}{3}}Y_{1,\pm 1} = \mp rC_{\pm 1}^{(1)}$$

$C_m^{(l)} = \sqrt{4\pi/2l+1}\,Y_{l,m}(\theta,\varphi)$ is Racah's spherical Tensor operator [88] and is introduced here to simply eliminate the numerical factor.

Dividing the transition rate (Fermi's golden rule) by the photon flux gives the absorption cross- section in the dipole approximation:

$$\sigma^{\pm} = 4\pi^2\hbar\omega\alpha\sum_{f,i}\left|\left\langle f\left|\mp rC_{\pm1}^{(1)}\right|i\right\rangle\right|^2\delta\left(E_f - E_i - \hbar\omega\right)$$

where α is Sommerfeld's fine-structure constant. The asymmetry of the circular dichroic signal is then given as $A = \frac{\sigma^{+}-\sigma^{-}}{\sigma^{+}+\sigma^{-}}$

According to dipole selection rules the transition matrix elements are non-zero only if $\Delta l = l_f - l_i = \pm 1$ and $\Delta m_s = 0$ and $\Delta m_l = +1$ for left circular polarization (positiv helicity) and $\Delta m_l = -1$ for right circular polarization (negativ helicity). The absorption intensity is given as:

$$I \propto \sum_{f,i}\left|\langle\psi_f|x \pm iy|\psi_i\rangle\right|^2\delta\left(E_f - E_i - \hbar\omega\right)$$

Because of the spin-orbit coupling the six 2p states are split (at least in the final state configuration (see above)). These are eigenstates of total angular momentum j^2 and j_z with quantum numbers j and m_j. The new states $|j,m_j\rangle$ are then related to the uncoupled states $|l,m_l\rangle$ and $|s,m_s\rangle$ by the relation:

$$|j,m_j\rangle = |ls;j,m_j\rangle = \sum_{m_l m_s}\langle ls, m_l m_s|j,m_j\rangle|l,m_l\rangle|s,m_s\rangle = \sum_{m_l m_s}\langle ls, m_l m_s|j,m_j\rangle|l,m_l;s,m_s\rangle$$

where $j = l \pm s$ and $m_j = m_l + m_s$. $\langle ls, m_l m_s|j,m_j\rangle$ are the Clebsch-Gordon coefficients. For the level with maximum values of the quantum numbers j and m_j the Clebsch-Gordon coefficient is 1. The others can be calculated with the aid of ladder operators or simply by use of recursion formulas deduced with those [89]. Many people use to prefer the Wigner "3j" symbol instead of the Clebsch-Gordon coefficients because of its higher symmetry. Both coefficients are related by:

$$\begin{pmatrix} j_1 & j_2 & J \\ m_1 & m_2 & -M \end{pmatrix} = \frac{(-)^{j_1-j_2+M}}{\sqrt{2J+1}}\langle j_1 j_2 m_1 m_2|J,M\rangle$$

If it is assumed that the overlap of the radial part of the wavefunction is constant and the same for the L_2 and the L_3 edge, and since the dipole operator does not act on the spin part of the wavefunction the polarization dependence of the transitions is entirely contained in the angular parts of the matrix elements: $\left\langle l = 2, m_l \pm 1\left|\mp C_{\pm1}^{(1)}\right|l = 1, m_l\right\rangle$. Analytical solutions to this problem are known [90]. The calculated values with the wave functions given above are summarized in the following table:

J	m_j	m_l	m_s	$30M^2$	M^2	$(CG)^2$	I_{calc}	I%
$^1/_2$	$-^1/_2$	-1	$^1/_2$	2	$^1/_{15}$	$^2/_3$	$^2/_{45}$	10
$^1/_2$	$-^1/_2$	0	$-^1/_2$	6	$^1/_5$	$^1/_3$	$^1/_{15}$	15
$^1/_2$	$^1/_2$	0	$^1/_2$	6	$^1/_5$	$^1/_3$	$^1/_{15}$	15
$^1/_2$	$^1/_2$	1	$-^1/_2$	12	$^2/_5$	$^2/_3$	$^4/_{15}$	60
$^3/_2$	$-^3/_2$	-1	$-^1/_2$	2	$^1/_{15}$	1	$^1/_{15}$	7,5
$^3/_2$	$-^1/_2$	-1	$^1/_2$	2	$^1/_{15}$	$^1/_3$	$^1/_{45}$	2,5
$^3/_2$	$-^1/_2$	0	$-^1/_2$	6	$^1/_5$	$^2/_3$	$^2/_{15}$	15
$^3/_2$	$^1/_2$	0	$^1/_2$	6	$^1/_5$	$^2/_3$	$^2/_{15}$	15
$^3/_2$	$^1/_2$	1	$-^1/_2$	12	$^2/_5$	$^1/_3$	$^2/_{15}$	15
$^3/_2$	$^3/_2$	1	$^1/_2$	12	$^2/_5$	1	$^2/_5$	45

where M^2 is the square of the respective matrix element and $(C G)^2$ the square of the corresponding Clebsch Gordan coefficient. $I_{calc} = M^2 (C G)^2$ is the relative contribution to the absorption intensity (also given in %). These data reproduce the values as given in Fig.16.
So far, we have assumed that all d states are empty and accessible by transitions. This is not the case for a magnetic material, but we can now within this simple model sort out all occupied d states and calculate the XMCD signal. (Transitions to the occupied states are forbidden by the Pauli exclusion principle). For the simple case that all $m_s = -^1/_2$ states are occupied (half filled d band: L = 0) at the L_2 edge we get a 25 % σ_+ transition intensity:

$$I_{\sigma^+} = \left(\frac{1}{15}+\frac{2}{45}\right)\mathfrak{R}^2 = \frac{1}{9}\mathfrak{R}^2$$

and for σ_- polarized light we get a 75% transition intensity

$$I_{\sigma^-} = \left(\frac{1}{15}+\frac{4}{15}\right)\mathfrak{R}^2 = \frac{1}{3}\mathfrak{R}^2$$

Therefore, for this ground state occupation the dichroism at the L_2 edge is:

$$\Delta I_{L_2} = I_{\sigma^+} - I_{\sigma^-} = -\frac{2}{9}\mathfrak{R}^2$$

Similarly, at the L_3 edge we get:

$$I_{\sigma^+} = \left(\frac{1}{15}+\frac{2}{45}\right)\mathfrak{R}^2 = \frac{1}{9}\mathfrak{R}^2$$

and

$$I_{\sigma^-} = \left(\frac{1}{15} + \frac{4}{15}\right)\mathfrak{R}^2 = \frac{1}{3}\mathfrak{R}^2$$

The dichroism at the L_3 edge is:

$$\Delta I_{L_2} = I_{\sigma^+} - I_{\sigma^-} = \frac{2}{9}\mathfrak{R}^2$$

that is, in this simple case the dichroic signal at the L_3 and L_2 edges has equal magnitude but opposite sign as expected for a spin only signal. (The orbital momentum for a half filled band is zero.) In this example we have from a given ground state occupation deduced the corresponding XMCD- signal. The sum rules discussed in chapter 5 invert this procedure and deduce the ground state occupation from the observed XMCD signal.

References

[1] S. Cramm, IFF Spring School Vol. 38, 2007

[2] C.S. Fadley, IFF Spring School Vol. 38, 2007

[3] B.K. Agarwal, *X-ray Spectroscopy, An Introduction*, Springer Verlag Berlin, Heidelberg, New York (1979)

[4] D.C. Koningsberger and R. Prins(Ed.), *X-ray Absorption - Principles, Applications, Techniques of EXAFS, SEXAFS and XANES*, John Wiley & Sons, New York (1988)

[5] J. Stöhr, *NEXAFS Spectroscopy*, Vol. 25 of Springer Series in Surface Science, Springer Verlag, Berlin, (1996)

[6] A.S. Schlachter and F.J. Wuilleumier (Ed.), *New Directions in Research with Third-Generation Soft X-Ray Synchrotron Radiation Sources*, Kluwer Academic Publishers, Dordrecht, Boston, London (1994)

[7] F. Hippert, E. Geissler, J.L. Hodeau, E.Lelievre, J.R. Regnard (Ed.), *Neutron and X-ray Spectroscopy*, Springer Dordrecht (2006).

[8] B. Lengeler in: *Synchrotronstrahlung zur Erforschung kondensierter Materie*, 23. IFF-Ferienkurs, Forschungszentrum Jülich (1992), ISBN 3-89336-088-3 (in German)

[9] U. Döbler, in: *Synchrotronstrahlung zur Erforschung kondensierter Materie*, 23. IFF-Ferienkurs, Forschungszentrum Jülich (1992), ISBN 3-89336-088-3 (in German)

[10] W. Zinn, in: *Synchrotronstrahlung zur Erforschung kondensierter Materie*, 23. IFF-Ferienkurs, Forschungszentrum Jülich (1992), ISBN 3-89336-088-3 (in German)

[11] G. Schütz,and P. Fischer, in: *Magnetismus von Festkörpern und Grenzflächen*, 24. IFF-Ferienkurs, Forschungszentrum Jülich (1993), ISBN 3-89336-110-3 (in German)

[12] H. Ebert and Ya. Perlov, in: *Magnetische Schichtsysteme*, 30. IFF-Ferienkurs, Forschungszentrum Jülich (1999), ISBN 3-89336-235-5 (in German)

[13] S. Eisebitt, in: in: *Magnetische Schichtsysteme*, 30. IFF-Ferienkurs, Forschungszentrum Jülich (1999), ISBN 3-89336-235-5 (in German)

[14] F.U. Hillebrecht, in: *Magnetism goes Nano*, 36. IFF-Ferienkurs, Forschungszentrum Jülich (2005), ISBN 3-89336-381-5

[15] R. Stumm von Bordwehr, Ann. Phys. Fr. **14**, 377(1989) [16] see contribution of C. M.

Schneider to this Spring School

[17] J. A. Victoreen, J. Appl. Phys. **14**, 95 (1943); ibid. **19**, 855(1948) [18] W. Kossel,Phys.Z. **18**, 240 (1917)

[19] J. Stöhr and Y. Wu, in [6]

[20] G.K. Woodgate, *Elementary Atomic Structure*; Mc Graw Hill, London (1970), p.36ff

[21] H. Moseley, Phil. Mag. **26**, 1024 (1913), 703 (1914)

[22] A. Dauvillier, Compt. Rend. Acad. Sci. **174**,1347 (1922); G. Urbain, ibid p. 1349 [23]

http://www-ssrl.slac.stanford.edu/sbsummerschool/studentsonly/
Brown 2005 environ science.pdf;

[24] D. T. Attwood http://www-ssrl.slac.stanford.edu/sbsummerschool/studentsonly/

[25] D. T. Attwood, *Soft X-rays and extreme ultaviolett radiation principles and applications*, Cambridge Univ. Press 2000

[26] W. Mehlhorn, J. Electr. Spectr. Relat. Phenom. **93**,1-15(1998) [27] M. F. Chung and J. H. Jenkins, Surf. Sci., **22**, 479-485 (1970)

[28] P. A.Bennett, J. C.Fuggle, F.U. Hillebrecht, A. Lenselink, and G. A. Sawatzky, Phys. Rev. **B 27**,2194(1983)

[29] B. Lengeler, in: [7]

[30] Alojz Kodre, Iztok Arčon, and Jana Padežnik Gomilšek, Acta Chim. Slov., **51**, 1-10, (2004)

[31] De Fanis A, Saito N, Yoshida H, Senba Y, Tamenori Y, Ohashi H, Tanaka H and Ueda K, Phys. Rev. Lett. **89**, 243001 (2002); K. Ueda J.Phys.B: At. Mol. Opt. Phys. **36**, R1 (2003)

[32] U. Fano, Phys. Rev. **124**, 1866 (1961); U. Fano and J. W. Cooper, Phys. Rev. **A 137**, A1364 (1965)

[33] M. Oura, Y. Tamenori, T. Hayaishi, Y. Kanai, H. Yoshii, K. Tsukamoto, and F. Koike, Phys. Rev **A 70** 022710 (2004)

[34] M. Kato, Y. Morishita, F. Koike, S. Fritzsche, H. Yamaoka, Y. Tamenori, K. Okada, T. Matsudo, T. Gejo, I. H. Suzuki, and N. Saito, J. Phys. B: At. Mol. Opt. Phys. **39** 2059-2069 (2006)

[35] C.T. Chen, Y. Ma, F.Sette,Phys. Rev. **A 40**, 6737 (1989)

[36] figure taken from ADVANCED LIGHT SOURCE Activity Report 2001, p44 see also: W.C. Stolte et al., Phys. Rev. Lett. **86**, 4504 (2001)

[37] J.D. Dehmer and D. Dill, J. Chem. Phys. **65**, 5327 (1976)

[38] S.R. Bare, from: w3.rz-berlin.mpg.de/~ jentoft/lehre/bare_xas_271006.pdf

[39] Matthew Newville, *Fundamentals of XAFS*, University of Chicago, http://cars9.uchicago.edu/~newville/

[40] K. M. Kemner, S. D. Kelly, K. A. Orlandini, A. I. Tsapin, M. G. Goldfeld, Y. D. Perfiliev, and K. H. Nealson, J. Synchrotron Rad. **8**, 949 (2001)

[41] J.G. Chen, Surface Science Reports **30**, 1-152 (1997)

[42] J. Stöhr, K. Baberschke, R.Jaeger, R. Treichler, S. Brennan, Phys. Rev. Lett. **47**, 381 (1981)

[43] E. A. Stern, in: [4]

[44] J.J. Rehr, R.C. Albers, Rev. Mod. Phys. **72**, 621 (2000)

[45] J.E. Penner-Hahn, Coord. Chem. Rev. **190-192**, 1101 (1999)

[46] G. Schütz, W. Wagner, W. Wilhelm, P. Kienle, R. Zeller, R. Frahm, G. Materlik, Phys. Rev. Lett. **58**, 737 (1987)

[47] J. Stöhr, R. Nakajima, IBM J. Res. Develop. **42**, 73(1998) [48] J. Stöhr, J. Electr. Spectr.

Relat. Phenom. **75**, 253 (1995)

[49] J. Stöhr, H. C. Siegmann, *Magnetism – From Fundamentals to Nanoscale Dynamics*, Springer Verlag, Berlin, Heidelberg, New York (2006)

[50] J. Goulon, C. Goulon-Ginet, A. Rogalev, V. Gotte, C. Malgrange, C. Brouder, C. R. Natoli, J. Chem. Phys. **108**, 6394 (1998)

[51] T. Funk, A. Deb, S. J. George, H. Wang, S. P. Cramer, Coord. Chem. Rev. **249**, 3 (2005) [52] C. T. Chen, Y. U. Idzerda, H.-J. Lin, N. V. Smith, G. Meigs, G. H. Ho, E. Pellegrin, and F. Sette, Phys. Rev. Lett. **75**, 152 (1995)

[53] W. Kuch, *Abbildende magnetische Mikrospektroskopie*, Habilitationsschrift, Martin-Luther-Universität Halle-Wittenberg(2002), http://sundoc.bibliothek.uni-halle.de/habil- online/02/03H047/index.htm

[54] U. Fano, Phys. Rev. **178**, 131(1969); addendum Phys. Rev. **184**, 250 (1969) [55] D. T. Pierce, F. Meier, Phys. Rev. Lett. **13**, 5484 (1976)

[56] J. Kessler, *Polarized Electrons*, Springer Verlag, Berlin (1985)

[57] D. T. Pierce, *Atomic, Molecular and Optical Physics: Charged Particles*, Academic Press

(1995) 1

[58] G. F. Hanne, *Polarisierte Elektronen*, www.uni-muenster.de/Physik.PI/Hanne/skripte.html] [59] F. Baudelet, in: [7]

[60] Wolfgang Kuch, Physica Scripta T**109**, 89-95, 2004

[61] W. Kuch, *Imaging Magnetic Microspectroscopy*, in: H. Hopster and H. P. Oepen (Eds.), *Magnetic Microscopy of Nanostructures*, p. 1-28, Springer, Berlin (2004). ISBN 3-540-40186-5, http://www.mpi-halle.mpg.de/mpi/publi/ki/2004/abs pdf/5587 04.html

[62] C. M. Schneider, D. Venus, and J. Kirschner, Phys. Rev. B 45, 5041 (1992)

[63] B. T. Thole, P. Carra, F. Sette und G. van der Laan, Phys. Rev. Lett. **68**, 1943 (1992). [64]

P. Carra, B. T. Thole, M. Altarelli und X. Wang, Phys. Rev. Lett. **70**, 694 (1993).

[65] J. Stöhr and H. König, Phys. Rev. Lett. **75**, 3748 (1995) [66] M. Altarelli, Phys. Rev. **B**

47, 597 (1993)

[67] T. Jo, J. Phys. Soc. Japan **62**, 1814 (1993)

[68] A. Ankudinov, J. J. Rehr, Phys. Rev. **B 51**, 1282 (1995)

[69] M. Sacchi and J. Vogel, p. 87 in: E. Beaurepaire, F Scheurer, G. Krill, and J.-P. Kappler (Eds.), *Magnetism and Synchrotron Radiation*, Springer-Verlag, Berlin-Heidelberg (2001)

[70] H. Ebert, Rep. Prog. Phys. **59**, 1665 (1996)

[71] P. Bruno, Phys. Rev. **B 39**, 865 (1989)

[72] A. Dallmeyer, C. Carbone, W. Eberhardt, C. Pampuch, O. Rader, W. Gudat,P. Gambardella, and K. Kern, Phys. Rev. **B 61**, R5133 (2000)

[73] P. Gambardella, S. S. Dhesi, S. Gardonio, C. Grazioli, P. Ohresser, and C. Carbone, Phys. Rev.Lett. **88**, 047202 (2002)

[74] P. Gambardella, S. Rusponi, M. Veronese, S. S. Dhesi, C. Grazioli, A. Dallmeyer, I. Cabria, R. Zeller, P. H. Dederichs, K. Kern, C. Carbone, H. Brune, Science **300**, 1130 (2003)

[75] I. Cabria, B. Nonas, R. Zeller, and P.H. Dederichs, Phys. Rev. **B 65** 054414 (2002)

[76] P. Gambardella, S. Rusponi, M. Veronese, S. S. Dhesi, C. Grazioli, A. Dallmeyer, I. Cabria, R. Zeller, P. H. Dederichs, K. Kern, C. Carbone, H. Brune, Science **300**, 1130 (2003)

[77] J.T. Lau, A. Föhlisch, R. Nietubyć, M. Reif, and W. Wurth, Phys. Rev. Lett. **89** 057201

(2002)

[78] J .T. Lau, A. Föhlisch, M. Martins, R. Nietubyć, M. Reif and W. Wurth, New Journal of Physics **4**, 98.1 (2002)

[79] P.S. Bechthold, in: *Magnetism goes Nano*, 36. IFF-Ferienkurs, Forschungszentrum Jülich (2005), ISBN 3-89336-381-5;
www.fz-juelich.de/iff/src/fs/2005/download/C6 Bechthold FS05.pdf

[80] B. T. Thole, G. van der Laan, and G. A. Sawatzky, Phys. Rev. Lett. **55**, 2086 (1985)

[81] G. van der Laan, B.T. Thole, G.A. Sawatzky, J.B. Goedkoop, J.C. Fuggle, J.-M. Esteva, R. Karnatak, J.P. Remeika, H.A. Dabkowska, Phys. Rev **B 34**, 6529 (1986)

[82] P. Curie, Journal de Physique **3**, 401 (1894) [83] F. de Groot, and J. Vogel, in: [7]

[84] J. Stöhr, www-ssrl.slac.stanford.edu/stohr/xmcd.htm

[85] D. Alders, J. Vogel, C. Levelut, S. D. Peacor, T. Hibma, M. Sacci, L. H. Tjeng, C. T. Chen, G. van der Laan, B. T. Thole, and G. A. Sawatzky, Europhys. Lett. **32**, 259 (1995).

[86] figure taken from: J. Stöhr, S. Anders, IBM J. Res. Develop. **44**, 535 (2000) [87] J. L.

Erskine and E. A. Stern, Phys. Rev. **B 12**, 5016 (1975)

[88] B.W. Shore and D.H. Menzel, *Principles of Atomic Spectra*, John Wiley and Sons, New York (1968)

[89] A. Messiah, *Quantum Mechanics, Vol. II*, North Holland Publishing Company, Amsterdam (1970)

[90] H.A. Bethe, E.E. Salpeter, *Quantum Mechanics of One and Two Electron Atoms*, Plenum, New York (1977)